CHARACTERIZATION AND IMPACT OF THERMAL CONDUCTIVITY OF STAINLESS STEEL 316L EMPLOYED IN ADDITIVE MANUFACTURING

CARLOS ABEL ROJAS DORANTES

A THESIS SUBMITTED TO THE FACULTY OF GRADUATE STUDIES IN PARTIAL FULFILLMENT OF THE REQUIREMENTS FOR THE DEGREE OF MASTER OF APPLIED SCIENCE

GRADUATE PROGRAM IN MECHANICAL ENGINEERING

YORK UNIVERSITY

TOTONTO, ONTARIO

DECEMBER 2020

Abstract

The main objective of this research was to develop new methods to improve the mechanical properties of 3D printed metal parts by controlling the heat transfer mechanisms involved in the melting and solidification of powder particles. A number of experiments were carried out to study the parameters involved in the process. The first part of the work was dedicated to the measurement of effective thermal conductivity in 316L stainless-steel powder. The results showed that controlled samples had important increments in thermal conductivity. The experimental setup was based on a steady-state analysis, designed to safely expose the sample up to 1000 °C. The best result was obtained from the 10% compacted sample, whose thermal conductivity was double that of the reference sample. In the second part of this work, simulations were performed of a laser track over a powder bed. The results obtained from the thermal conductivity experiments were compared with those from analytical models. The thermal behaviour of the powder displayed an important decrement in temperature gradients. Moreover, analysis of subsequent laser tracks showed important improvements under low energy density. In summary, the theorical findings of this work can help to reduce and control defects formed in the melting and solidification stages of the manufacturing process by limiting temperature gradients and improving thermal distribution.

Acknowledgements

I am very thankful for doing a master's in science degree in the department of mechanical engineering under the supervision of Dr. Aleksander Czekanski. I am very grateful that he gave an amazing opportunity and support to conduct my research. I was also very glad of meeting brilliant members of IDEA-LAB, that provide me help, guidance, and advice. Without them I would not be able to succeed in my research. There are not words to describe how grateful I am.

I dedicate this thesis to my family, that in the last years were very supportive with my decisions, even if I was far from home. My mom Hilda, my dad Carlos, my brother Daniel, and my sister Ana. Also, to my friends that were encouraging in my time in Canada. Finally, to my professors that guide me all the years that I studied. In addition, I am thankful for my colleagues and friends from the grad area of mechanical engineering and the recreational group activities that we had. Finally, I am grateful to the Natural Sciences and Engineering Research Council of Canada (NSERC) for providing important financial support to our research group.

Table of contents

List of tables

List of figures

List of abbreviations

AM	additive manufacturing
ASTM	American Society for Testing and Materials
DED	directed energy deposition
DEM	discrete element method
DMLS	direct metal laser sintering
EBM	electron beam melting
FEA	finite element analysis
PB	powder bed
PBF	powder bed fusion
SLS	selective laser sintering
SS	stainless steel

List of symbols

A	area
V_{avg}	average velocity
vi	average viscosity
λ	bulk thermal conductivity
r_{c}	contact radius
x	contact size ratio
n	coordination number
ρ	density of the fluid
D	diameter
L	distance between thermocouples
μ	dynamic viscosity
λ_{e}	effective thermal conductivity
Ω	electrical resistance
τ	half-period of the pulse of heating current
s	hatching distance
q	heat flux
F	heat flux
φ_{q}	heat flux density
Q	heating power
IED	input energy density
E_v	laser energy density
P	laser power input
h	layer thickness
LPH	liters per hour

$\dot{m}$	mass flow
r_{p}	particle radius
ρ	relative density
Re	Reynolds number
v	scan speed
c_p	specific heat
S	surface contact
T	temperature
T_a	temperature after furnace
T_b	temperature before furnace
k	thermal conductance
k	thermal conductivity
λ_{s}	thermal conductivity of the dispersed phase
λ_{g}	thermal conductivity of the matrix
α	thermal diffusivity
ΔT	thermal gradient between thermocouples 1 and 2
S	thermal resistance
t	time
V	voltage
f_{s}	volume fraction of the dispersed phase
C	volumetric heat capacity

Chapter One: Introduction

1.1 Background

This research focuses on improving the mechanical properties of 3D printed metal parts. Additive manufacturing (AM) is used to build such parts layer by layer, allowing users to generate parts with complex geometries [1]. As a result, parts made with AM can be optimized to reduce their weight while maintaining adequate support for established loads [2].

While mass production is not feasible when production times are compared with those of traditional manufacturing, several sectors that require more customized solutions favour AM. For instance, AM is usually associated with prototyping and do-it-yourself solutions, but metal AM is more related to industrial fields like aerospace and medicine [3][4].

Different AM processes are used to produce 3D printed metal parts. Some of the most well-developed technologies are based on powder bed fusion. Powder bed fusion processes all operate in a similar way, and the equipment for these processes share the following basic elements: at least one heat source to fuse the material (a laser or electron beam); a movement controller to guide the heat source; and a system to control the powder's layers [3].

However, the limitations of AM include lacking mechanical properties when compared with traditional methods. One example is directly attributed to the layer-by-layer building method, in which the bonds that connect the different layers do not have the same mechanical properties compared with the individual printed layers [5].

Other defects in 3D printed parts are related to the insufficient amount of material and/or laser energy. During the building process, since the behaviour of the powder cannot be restricted, some particles will properly melt or sinter, while other particles will be thrown off the laser path. As a result, the laser paths are not always perfect aligned. In some regions, the material will not receive enough heat energy to melt; other regions will not have enough material, creating more porosity than desired [6][7].

A number of experiments have been conducted to identify the effects of printer parameters on the final mechanical properties of 3D printed parts [8]. As a result, several attempts have been made to predict the properties of materials using computer simulations and algorithms. In recent years, few experiments have explored powder and preprocessed materials [9]. A popular research topic involving powdered materials in AM is the reusability of the powder after a certain number of processes. Nevertheless, only few studies are related to heat transfer and dispersion between particles [10].

1.2 Research Gaps

In recent years, the majority of research papers in AM focused on parametric analysis and simulations. Thanks to these extensive investigations, the field of AM has developed a greater understanding of the effect of printing process parameters on the microstructure and mechanical properties of 3D printed parts, including fatigue, tensile strength, Young's modulus, etcetera. However, simulations are focused on predicting the final properties of parts based on several experiments performed under different conditions.

One of such process parameters, thermal conductivity, is a property that changes with temperature that determine the capability of transfer heat. Yet few experimental results on powders exist because of the complexity and number of variables involved in the powder bed fusion process. Moreover, experiments can only be performed within a certain temperature range, which in general is not close to the sintering point, the temperature at which the material starts to partially melt. Therefore, it is difficult to know how thermal conductivity is influenced when a contact point starts to become a connection.

A thorough scan of the literature reveals that plenty of studies have been done on the subject of AM. However, the number of published research articles decreases as the price of AM equipment and supplies increases. For example, using a search platform called Scopus, the number of articles using the tag "additive manufacturing" was found to be nearly 30,000; adding "metal" to the search query decreased the number of articles to just over 6,000. When the tag "powder" was added to the search query, it further decreased the number of articles to less than 3,000. Finally, after including additional tags to narrow the search to experiments on 316L grade stainless steel (SS-316L), fewer than 20 articles remained. At the end, the number of papers published on the proposed topic represents ~0.06% of all articles on AM.

1.3 Justification

Parametric studies on AM are now reaching the limit of their potential. Some studies are reporting that printed parts can get densities of almost 100% and outstanding mechanical properties. However, 3D printed parts still lack the same reliability as parts fabricated using traditional manufacturing methods. From that perspective, opportunities remain to optimize the AM process to produce changes that exceed those that can be made by a user who merely modifies process parameters. Optimizing the material used in AM can result in significant improvements. Uniform melting of material will create better consolidation between layers. A study of the heat transfer in powder beds is needed to determine the best configuration of powder structures. Moreover, results can also be achieved through more accurate simulations, when one takes into account that thermal conductivity is a factor that changes with temperature.

The thermal conductivity of powder has not been widely studied at high temperatures. The limitations of some methods mean that thermal conductivity can be measured only at ambient temperature, while other methods give the option of increasing the temperature but not enough to deform the material. Obtaining experimental results is important for comparing analytical approximations developed over the years, to allow corrections to be made in possible variables of ratios in analytical models.

1.4 Research Objectives

The main goal of the present research was to find methods to improve the reliability of parts made through AM. Given that so many different stages of the AM process can be improved, first the topic was narrowed down to study powdered materials and its thermal behaviour, then the research question was defined as follows: How can the fusion process of powder particles be improved? to address the research question the following objectives were selected:

1. Measure the effective thermal conductivity of powders
    - Identify the effect of different particle densities
    - Measure the thermal conductivity at different temperature
2. Simulate and study the impact of thermal conductivity on powder beds
    - Study and compare thermal conductivity of particle models
    - Perform simulations of powder bed fusion process with obtained results

1.5 Research Methodology

According with the literature review, thermal conductivity at high temperatures must be measured. Therefore, a technique was designed to allow thermal conductivity to be measured at temperatures close to the sintering point using a tubular furnace and thermocouples resistant to high temperature.

Experiments were performed using different configurations of powder particles. Experimental samples were constructed using various techniques, including compacting, shaking, and gravity feeding.

Finally, the results obtained were used to perform simulations and define variables to complement previous analytical approximations. These results were compared with simulations generated using commercial software

1.6 Research Contributions

The purpose of this work was to conduct experiments with powdered metallic materials to determine their properties. There are many approaches to improving the properties of 3D printed parts by changing printing parameters. However, the optimization of the powder is not an approach that has been widely studied. While some simulations have attempted to recreate powder structures, there are not enough tridimensional models based on real powder particles.

In addition, this work uses experimental methods to quantify the thermal conductivity of different powder structures. To date, only a few experiments have been conducted to determine this magnitude, while others approaches performed analytical calculations considering a constant morphology and size. Therefore, designing a unique method would lead to a better re-creation of exposure during the real printing process.

1.7 Thesis Layout

The thesis is divided into six chapters. **Chapter 1** begins with the introduction and justification of the study. **Chapter 2** consists of a literature review, including a discussion of previous analytical models and approximations. **Chapter 3** examines the results of thermal conductivity powder characterization. **Chapter 4** presents finite element modeling of the experimental results. **Chapter 5** discusses the implications of this research and suggests future work.

Chapter Two: Literature Review

The advantages and applications of metal AM are growing in different fields, but the access to and reliability of AM are still limited. Cost and properties are important factors restricting its potential. Current applications are focused on industries with low-volume production and customized parts. More research is needed to develop the potential of AM for greater future impact.

This chapter presents background information to explain the importance of AM and its potential uses. Beginning with general information about AM, moves onto more specific PB processes, and ends with the characterization and properties of materials. Finally, this chapter also briefly touches upon analytical methods, which are used in later chapters to compare the experimental results obtained in the current research.

2.1 Additive manufacturing

AM is a fabrication method that adds material layer by layer to produce a final designed structure. There are several different methods of AM that add materials in incremental layers. These methods use a variety of options to join the materials, yielding printed parts with different properties and characteristics; as a result, the methods are divided into discrete categories of study [11]. Figure 2.1 shows the general methods classified by materials; however, other procedures share similar characteristics that can be further subclassified.

The present work focuses on powder processes. Nowadays, the application of metal powder in AM is not limited to PB-based processes. Other options include directed energy deposition (DED). Most of the processes based on PBF use similar arrangements of components, but the beam source and its capabilities are different. As a result, many processes might seem alike at first glance, but the properties of the materials and the process parameters will vary.

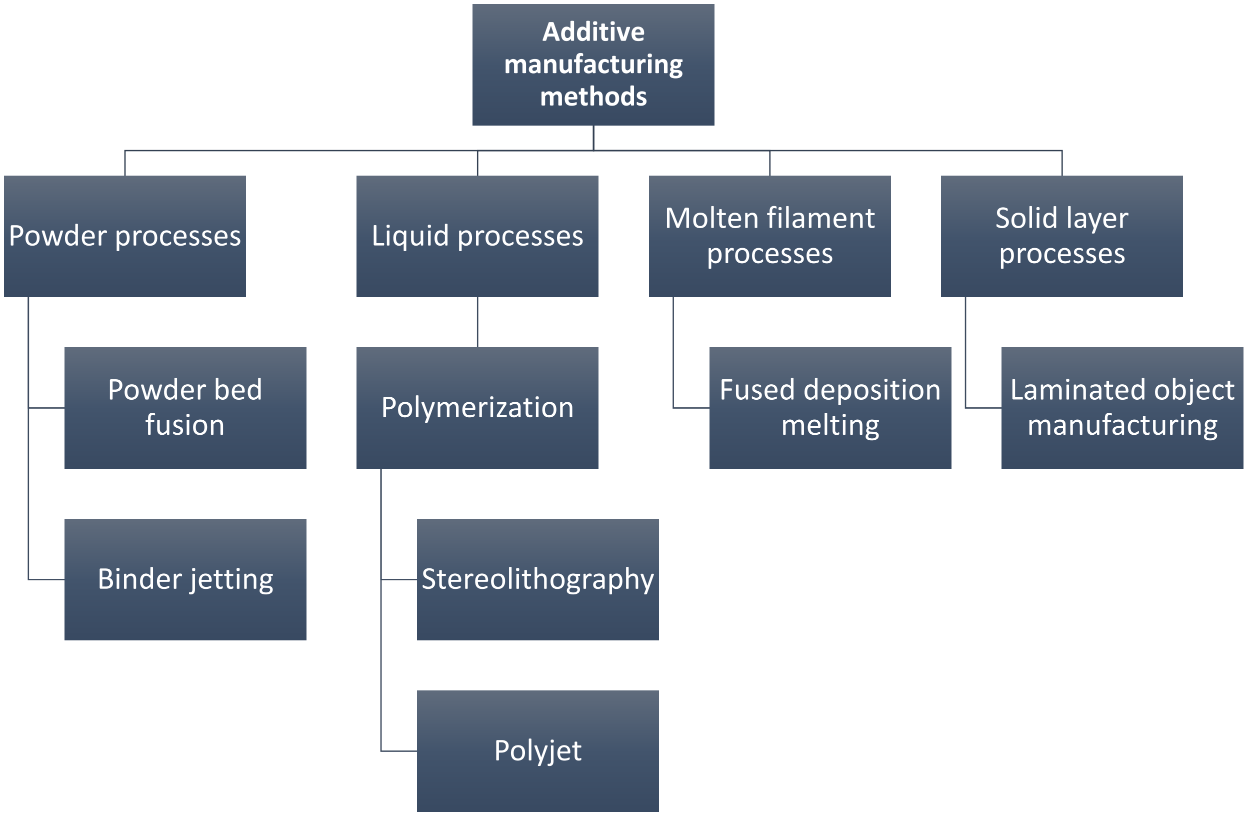

Figure 2.1. General additive manufacturing methods.

Overall, the operation of the AM process is similar regardless of the differences in the equipment. First, a model must be designed using CAD software. This model is exported to a file compatible with the equipment; the format is typically an STL file, also known as Standard Tessellation Language. In the software provided by the manufacturer, some parameters will be adjusted to the printing requirements. Finally, after conditioning the equipment, adding material, preparing and reviewing the operation code, and supervising the consumables and resources—the process would begin. Note that for safety reasons, most manufacturers do not allow users to manipulate advanced parameters and the materials used in the equipment.

The usual parameters controlled in the process, as illustrated in Figure 2.2, are as follows:

- Laser power
- Scanning speed
- Layer thickness, and
- Hatch spacing.

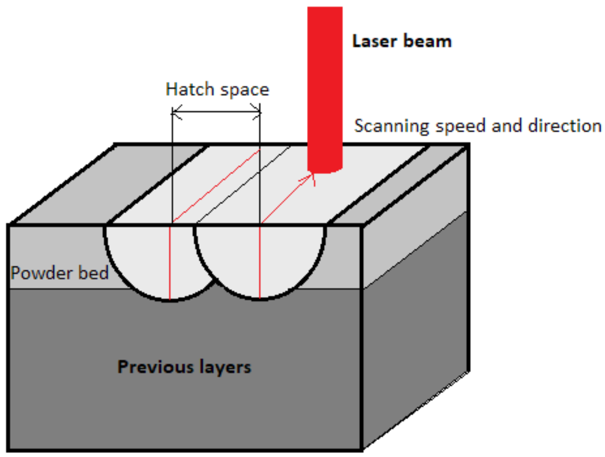

Figure 2.2. Printing parameters for additive manufacturing.

2.2 Current and future applications of additive manufacturing

The possibility of creating 3D printed parts with complex geometries is a key factor in reducing the weight of parts. For instance, the aerospace industry is very keen on reducing fuel consumption. Airbus, one of the biggest aircraft manufacturers, is working with design companies to reduce the weight of aircraft as much as possible [12], [13]. Bastian Schaefer, Cabin and Cargo Innovation Manager at Airbus Operations, claims that the company is aiming to reduce 50% of its greenhouse gas emissions by 2050 [12]. Using optimization methods, Airbus successfully reduced the weight of some structural components by 50% and also passed certification requirements (Figure 2.3) [14]. Moreover, AM helps to reduce the amount of material used: Airbus has claimed that the number of metal blocks that are currently machined by milling can de reduced [12]. Airbus has recognized that, in the future, an increasing number of parts for planes will be fabricated using AM, but challenges remain with the size of AM equipment and printing time and speed [12].

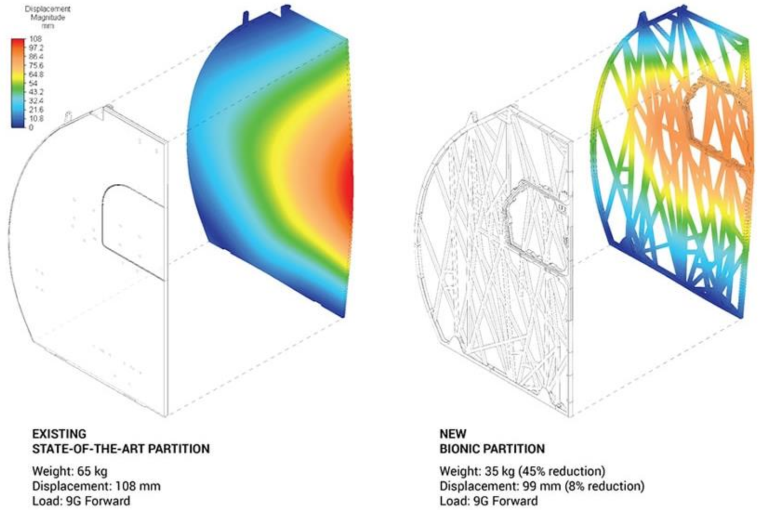

Figure 2.3. Airbus implementation of additive manufacturing and optimization [12].

In health care, AM is having a major impact owing to its ability to fabricate customized parts for patients (Figure 2.4). Additionally, AM has some flexibility during printing, as parts of different dimensions can be manufactured at the same time. Moreover, the number of parts can be optimized to be lower; for that reason, human error is reduced as well as potential element failures. Finally, AM is an excellent process for matching the mechanical features of the body by adding special mimicking features [15][16].

The benefits of AM extend beyond human applications. Veterinary AM implants have also been used and tested. Some applications are still under development, such as the design of spinal implants [17]. However, many applications have already been developed and successfully passed sanitary regulations [16][3][18], including dental frameworks, orthopedic implants, and surgical instruments.

Figure 2.4. Example of built implants [16], Copyright Renishaw plc.

AM also offers considerable benefits when it comes to the moulding process. AM is not able to produce many parts in a short time, and thus mass production is slow and limited compared with other methods like injection modeling. However, AM is able to produce moulds that can be used in other manufacturing methods (Figure 2.5). Moreover, there is the option of building special moulds with cooling channels to improve cooling and extend the life of the part [15]. In traditional methods, such channels are restricted to being straight lines within the mould and cannot be adjusted for optimal heat transfer.

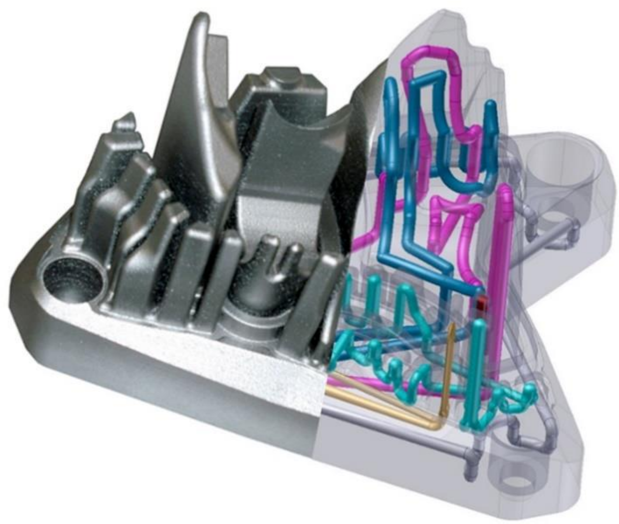

Figure 2.5. Example of a part containing cooling channels [15], Copyright Renishaw plc.

A prime example of using AM to achieve peak performance while reducing the weight of metal parts is the manufacturing of high-performance and luxury cars. These vehicles are not mass produced unlike other cars. Longer delivery and manufacturing times allow extra features to be added and lead to higher-quality vehicles. In the case of Formula 1 race cars, the number of cars and parts that are manufactured is limited, as complete cars are not built every day. Ferrari, one of the largest companies involved in Formula 1 racing, uses metal AM to achieve the goal of increasing the car's performance by reducing vehicle weight but maintaining the parts' reliability [19]. Bugatti, another manufacturer of high-performance cars, designed a new brake caliper to sustain the effects of braking over 375 km/h (Figure 2.6) [20]; they also designed a motor bracket with integrated water cooling for the Bugatti Chiron [21].

Figure 2.6. Caliper produced by Bugatti [20].

Another application for metal AM is jewelry manufacturing. AM offers new possibilities for creating jewelry with complex shapes. Designers can now innovate their work by adding features that were once almost impossible to produce using traditional methods [22]. Nevertheless, as with other materials, gold process parameters must be optimized. EOS, a manufacturer of 3D printing systems, has adapted the AM process for powder and developed the parameters to build parts of 18-karat gold [23] (Figure 2.7). However, other research has shown that optimal process parameters for pure 24-karat gold are harder to obtain because gold is a highly reflective material and lacks malleability [24].

Figure 2.7. Example of AM applied to jewelry manufacturing [22].

2.3 Additive manufacturing processes for metals

2.3.1 Selective laser sintering and direct metal laser sintering

Sintering is a process whereby material particles stick to one another. A laser beam is used as a heat source to create the necessary temperature to quickly form the particles into a solid mass without melting it. In selective laser sintering (SLS), a fully liquid melted material is not intended. Therefore, SLS is a process more commonly used for rapid prototyping and rapid tolling [25]. Figure 2.8 shows the schematic parts of an SLS system, where the laser, by either pulses or a continuous path, sinters powder particles. To add more material, the base will move down as more material is added on top using a roller or another feeder method designed by the manufacturer.

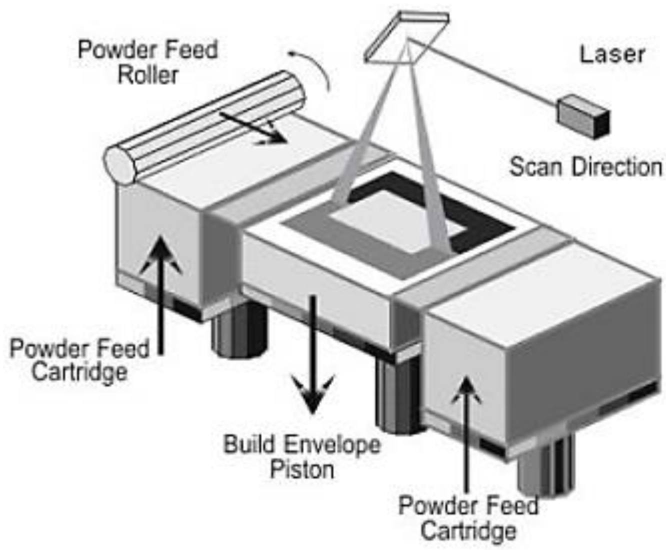

Figure 2.8. Standard selective laser sintering (SLS) system [25].

The principal difference between SLS and direct metal laser sintering (DMLS) is that DMLS applies only to metallic materials, while SLS is a more general classification. The equipment incorporates a high-power laser, which allow the user to sinter a wider number of materials. However, the temperature does not reach the total melting point of the particles.

The materials that are currently commercially available include [26][27]

- Stainless steel (17-4 PH, 316L)
- Aluminum AlSi10Mg
- Nickel alloys (625, 718)
- Titanium Ti64
- Cobalt–chrome (CoCrMo)
- MONEL K500, and
- Copper C18150.

2.3.2 Selective laser melting

Selective laser melting (SLM) is similar to DMLS (Figure 2.9), the distinguishing feature being that SLM can fully melt the material owing to its higher laser power, which produces denser parts without postprocessing [28]. Hence, SLM provides a great advantage over DMLS. That being said, more energy is also required to operate SLM, leading to increased production costs.

The company SLM Solutions has been working on the adaptability of SLM for large-scale production. Implementing a higher-power laser beam of 1 kW and an adequate PB temperature, the manufacturer was able to increase the process-related build-up rate more than 5 times [29].

The materials available for SLM are similar to those used for DMLS, although additional materials are available for SLM owing to the higher density of the resulting parts [30][31]:

- Iron-based alloys, stainless steel, and tooling steel: 316L (1.4404), 15-5PH (1.4545), 17-4PH (1.4542), alloy 1.2709, H13 (1.2344), and Invar 36
- Aluminum-based alloys: AlSi10Mg, AlSi7Mg0.6, AlSi9Cu3
- Titanium-based alloys: TiAl6V4 ELI (grade 23), TA15, Ti (grade 2)
- Cobalt-based alloys: CoCr28Mo6, SLM MediDent, and
- Copper-based alloys: CuNi2SiCr, CuSn10.

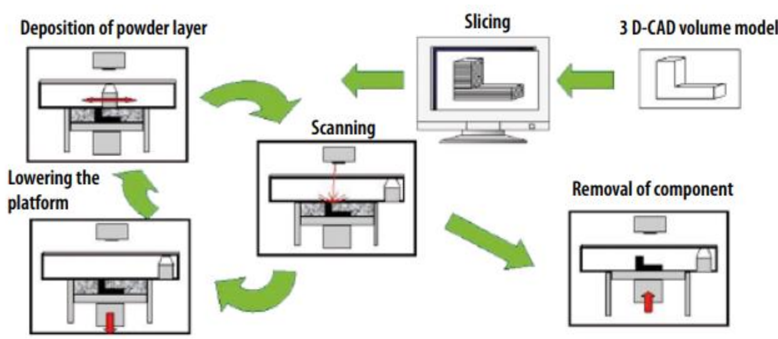

Figure 2.9. Selective laser melting process [29].

2.3.3 Electron beam melting

The concept of melting electrically conductive powder using an electron beam was invented in 1993. The company to develop the electron beam melting (EBM) method, Arcam AB, has continued developing EBM method since it was founded in 1997. Arcam AB was the first company to commercially produce an EBM machine for melting material. This machine was launched in 2002, and by 2007, the company had obtained FDA approval to manufacture implants. However, nowadays EBM is best suited for manufacturing large parts for the aerospace industry [32].

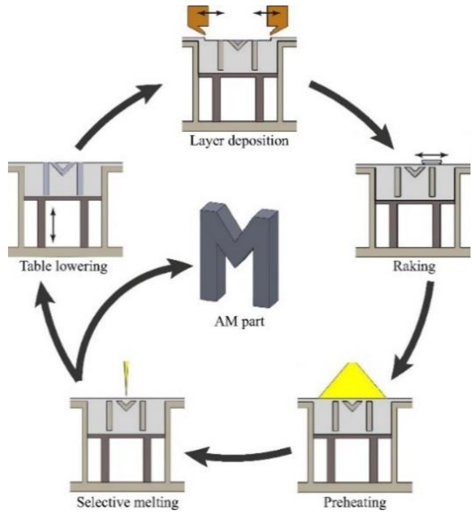

Figure 2.10. Electron beam melting process [33].

The process is very similar to SLS, where the electron beam takes the role of the laser to melt the material, as shown in Figure 2.10. The preheating process is performed by defocusing the beams and moving them at a high speed in the working layer of the powder bed (Figure 2.11) [34]. An important difference from other methods is that EBM is performed at a considerable vacuum pressure of 10^{-3} Pa [35]. As a result, any oxidation due to oxygen in the chamber is almost nonexistent, and the powders can therefore be reused for multiple cycles. The recommended strict postprocessing is limited to sand blasting the part to remove extra adhered powder particles. One important advantage is that EBM is one of a small number of processes that can achieve full melting of materials. Hence, the density of the material can almost reach the full bulk density.

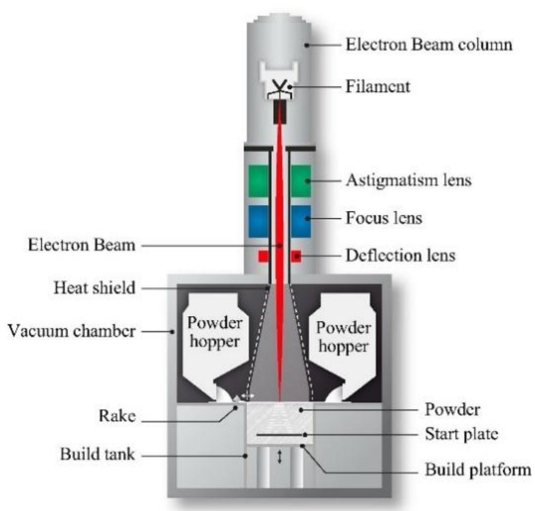

Figure 2.11. Diagram of an electron beam melting machine [33].

The materials available for us on EBM machines include [33]:

- Stainless steel (17-4)
- Tool steel (H13)
- Nickel-based superalloys (625 and 718)
- Cobalt-based superalloys (Stellite 21)
- Low-expansion alloys (Invar)
- Hard metals (NiWC)
- Intermetallic compounds
- Aluminum
- Copper, and
- Beryllium and niobium.

2.3.4 Selective LED-based melting

After the success achieved using laser beams to fuse particles, other attempts have been developed to overcome the disadvantages of lasers. Such was the case with researchers at Graz University of Technology (TU Graz), who recently announced that they had replaced the laser in the SLM machine with an LED (SLEDM). Moreover, parts in this machine are set to be built from top to bottom to reduce the amount of powder used, increasing the possibility that postprocessing can be performed while the part is being printed (Figure 2.12) [36].

The TU Graz researchers claimed to have designed an optimized method that reduces production time and postprocessing [36]. Using a complex arrangement of lenses, they designed a method that changes the size of the heat spot at an interval of 0.05 to 20 mm. As a result, the machine is able to process larger volumes of material in a shorter time [36].

Currently, the TU Graz research team has yet to publish the results detailing the final properties of the parts. However, they are starting to work on immediate applications in the fields of medical bioresorbable implants (using magnesium alloys) and sustainable mobility-producing bipolar plates for fuel cells [36].

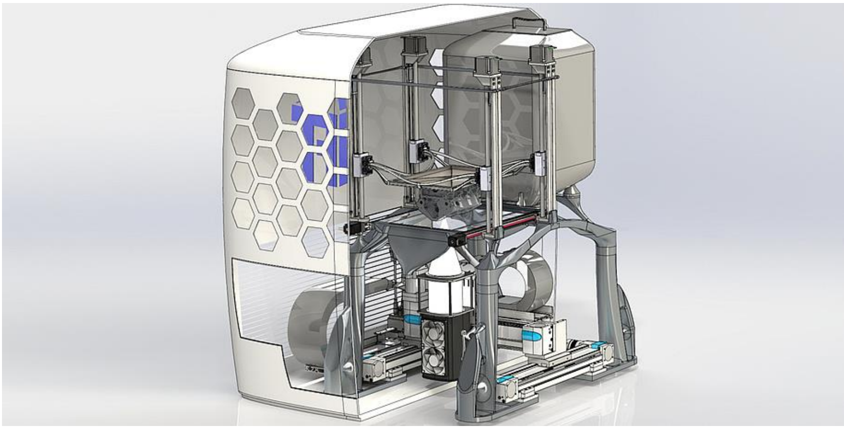

Figure 2.12. Selective LED-based melting printing system developed by TU Graz researchers [36].

2.3.5 Directed energy deposition

Directed energy deposition (DED) is an AM process that uses a nozzle to deposit material in a similar way to welding. Manufacturers name this method according to the specific characteristics of their machines; for instance, DED is known as laser engineered net shaping, directed light fabrication, and direct metal deposition. However, these machines are based on the same concept.

The DED process involves adding melted material, layer by layer, directly via a nozzle. Inside the nozzle, a flow of material (powder or wire) is melted by a heat source, covered by an inert shield gas (Figure 2.13). The energy melts the material around the spot, creating a melting pool. Subsequent layers are added on top of previous ones [37].

In general, the DED process is be defined by the method of feedstock and energy source used. Feeding the nozzle can be perform using two different shapes of materials, wire or powder based, while the energy to melt the material is usually deliver via a heat source such as a laser beam, electron beam, plasma, or electric arc (Figure 2.13) [37].

The major process parameters for laser-based DED are as follows [37]:

- Laser power
- Laser beam spot size
- Powder feed rate
- Scanning speed
- Carrier gas flow rate
- Clad angle
- Feedstock properties, and

- Layer dimensions.

In terms of mechanical properties, the process parameters directly affect the microstructure of the final printed part. As a result, the behaviour of DED parts will be different from that of a bulk part [37]. Process parameters can be modified to achieve some similarities in tensile testing, but what is generally detected is lower ductility in experimental results due to internal defects [38][39]. Studies in microhardness have shown variations in microstructure due to build direction. Moreover, higher microhardness has been detected in the external layers (first and last layers), while in the central layers microhardness was lower. Such variations were attributed to the thermal cycles during the DED process [37]. Finally, other defects that can be attributed to microstructure is the fatigue of the parts. The propagation of microfractures plays an important role when parts are under cycling loads. Some studies have shown that the propagation of fractures is more likely to happen in the plane direction and few in the tensile direction [39].

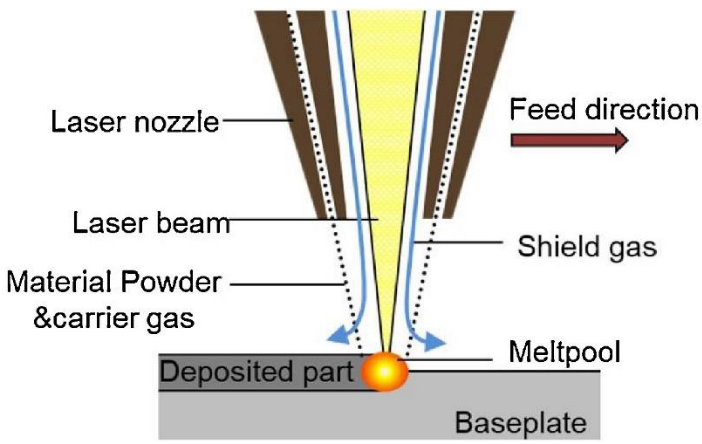

Figure 2.13. Directed energy deposition method [40].

2.3.6 Binder jetting

Binder jetting is another type of PB process. Like DMLS, binder jetting uses a PB with the material to build parts. However, instead of using a heat source like a laser, binder jetting uses a chemical substance, sometimes referred to as a binding agent [41], to paste the powder particles (Figure 2.14).

Important differences between binder jetting and DMLS include the presence of a larger number of nozzles to add the adhesive substance. For that reason, Hewlett Packard claims that binder jetting is faster than laser methods [41]. However, after applying the adhesive, light must be used to cure it. In addition, after building the so-called green part (see Figure 2.14), the part must be placed in a furnace to properly sinter the material and perform other common AM postprocessing steps.

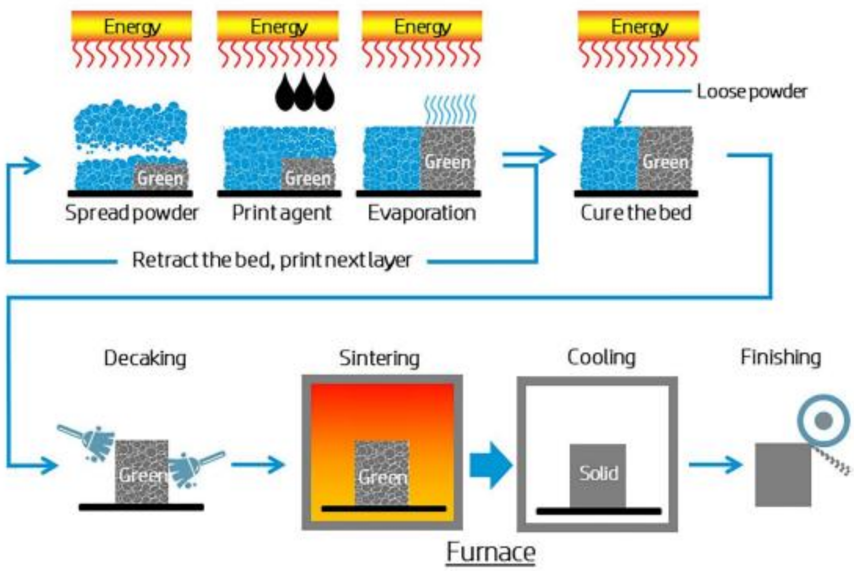

Figure 2.14. Binder jetting process [41].

Comparing the density of the parts, it is easy to see that the gaps in the green part between particles are not completely filled by the same material; for that reason, the number of voids after sintering the part in the furnace will be higher than the number resulting from using other methods [42].

Variation in PB layers leads to variation in properties and distortion in the postprocessing stage [42]. Mechanical properties are also worsened during the process. Results from experiments measuring Young's modulus for stainless steel 316 were compared before and after sintering, with Young's modulus decreasing from 200 to 4.07 GPa by the sintering process [43]. Such experiments show the large difference when a material is merely sintered. Moreover, the compared values are the highest obtained; other parameters were much lower than Young's modulus.

There is more flexibility in the types of materials that can be used in binder jetting machines than in equipment that uses beams to sinter powder. However, powders should still possess some characteristics, and the adhesive and its quantity should be adapted through experimental methods. The materials available on the market for binder jetting are as follows:

- Inconel
- Cobalt–chromium (CoCr)
- Copper, and
- Stainless steel.

2.4 Common defects in additive manufacturing

Defects occur in all manufacturing processes. However, the prevention and control of defects is an important consideration when commercializing manufactured elements. Parts are tested according to different standards to ensure that they will not fail when used as intended. In the case of AM, comparisons of tests vary significantly due to the variables involved in the process, making the value of these tests uncertain [44].

One common problem in AM is the porosity of materials. Early AM processes reported a high porosity (13%), while more recent AM processes had decreased the porosity to almost 0.00%. Reducing porosity is an important method to increase resistance to fatigue, due to the fact that cracks propagate between voids, accelerating the process of failure.

Other common issues are residual stresses, which are caused by the nonuniform consolidation of material initiated by temperature gradients. Residual stresses can lead to complete failure of parts.

2.5 Stainless steel 316L

In general, stainless steel is well recognized for its resistance to corrosion. This property comes from the addition of chromium to steel. The chemical composition defines the grade of steel and its properties. In addition to resistance to corrosion, the malleability of stainless steel is remarkable. Therefore, the use of stainless steel is widespread in many fields where clean materials are required that do not oxidize in their environments to prevent contamination, including the food industry, chemical equipment, heat exchangers, valves, aircraft, and so on [45].

Stainless steel 316L (SS-316L) is a low-carbon version of SS 316, but it has the same mechanical properties [46]. Adding carbon to steel alloys fundamentally changes the materials' properties. At higher concentration of carbon, it increases the hardness and strength of stainless steel; however, it also increases brittleness [47]. Therefore, SS-316L has an important advantage over SS-316 when ductility is compared.

Traditional methods are not capable of producing very small parts or parts with complex geometries. To do so, AM is an outstanding option. AM helps to decrease the number of parts needed to create a complex structure, simplifying the system.

2.5.1 Current applications of stainless steel 316L parts

The industrial purpose of SS-316L is to develop parts for use in many sectors, including automotive, aerospace, food, chemical, and jewellery (Figure 2.15) [27]. Parts are designed to take advantage of the features of AM and the properties of stainless steel. Applications are focused on replacing parts or elements in systems to create optimized versions. The potential of the materials and AM technology is clear to industry, but large-scale AM will take more time to develop.

Figure 2.15. Example of a printing process inside a RENISHAW AM 500.

SS-316L is a biocompatible material that is ideal for use in implants, as it is corrosion resistant and has good mechanical properties. The advantages of SS-316L over more common materials such as titanium include its lower cost as well as lower risk of toxicity [48]. Prosthetic shoulders, knees, and other body parts have now been successfully built using SS-316L. However, its lack of bioactive capabilities can produce premature failure of implants. Fortunately, a research group has designed a hydroxyapatite coating to increase the bioactive potential of SS-316L [48]. AM has transformed the implant industry. Patients are able to have customized parts manufactured that precisely meet their needs. Such parts can be generated using a magnetic resonance image of the patient's own body to build implants that are highly individualized [49]. Another critical advantage is the possibility of recreating porosity in an implant, which can help to hasten the processes of healing and adaptability [48].

2.5.2 Properties and challenges with stainless steel 316L

Considerable research has been conducted on optimizing the properties of parts made with SS-316L (Figure 2.16). Table 2.1 lists examples of experimental results with different parameters. Researchers have varied the parameters to build the parts, namely printing orientation, scanning speed, layer thickness, hatching distances, and power beam intensity. Moreover, some researchers have included postprocessing heat treatment. In many cases, the general properties have improved to produce parts as measured by ultimate tensile strength. However, yield strength generally increased the most drastically. The elongation at break was maintained within a close range, but some experiments showed a significant decrement, which can be attributed to the fast propagation of fractures caused by higher porosity.

Table 2.1. Mechanical properties of stainless steel 316L.

Source	Method	Ultimate tensile strength (MPa)	Yield strength (MPa)	Elongation at break (%)	Young's modulus (GPa)	Hardness (HRB)
United performance materials [50]	Bulk	485	170	40	190	96
AZO materials [46]	Bulk	500–700	170	40	193	95
Research paper [51]	Bulk	563	345	30	187	—
EOS [52]	DMLS	590–650	490–535	35–45		—
SLM Solutions [53]	SLM	588–637	470–510	41–45	171–178	95
Stratasys [54]	DMLS	640 ± 50	530 ± 60	40 ± 15	—	85
Research paper [51]	DMLS	680–717	473–496	28–30	180–193	—
Research paper [55]	SLM	570–720	470–550	40–55	—	—
Research paper [56]	LaserCUSING	550–588	405–478	23	—	—
Research paper [57]	DMLS	536–629	469–527	—	165–188	—

The limitations of this research work are related to the access to modify parameters or systems. Restrictions are not limited to the capabilities of the process, but to the confidentiality of the information. Some of the most relevant restrictions are as follows:

- Standardization. Some initial attempts have been made to generate protocols to manufacture parts with common materials. But the repeatability of results is a factor that is not completely within reach at this moment [6].
- Reflectivity of material. Some materials are not suitable to be processed using a laser or a concentrated heat source, as lasers can be reflected back causing damage of the unit. Therefore, material development should consider plenty of factors. For instance, despite the fact that the copper is highly reflective and does not absorb a lot of energy, some copper parts have been successfully produced, promising important developments for the use of copper parts in thermal applications [58].
- User restrictions. Modifications to the system that can be made by a user are limited because of the manufacturer's warranty. For example, in some experiments, instrumentation equipment was placed inside a chamber, but this idea was abandoned due to accessibility restrictions [59]. Another example is that, for some materials, a higher preheating temperature is more effective. However, manufacturers do not officially endorse replacing or modifying the heating unit [60].
- Process parameters are also limited to an optimal operational range by the manufacturer in order to prevent possible accidents. However, such restrictions also limit the development of materials from external companies.

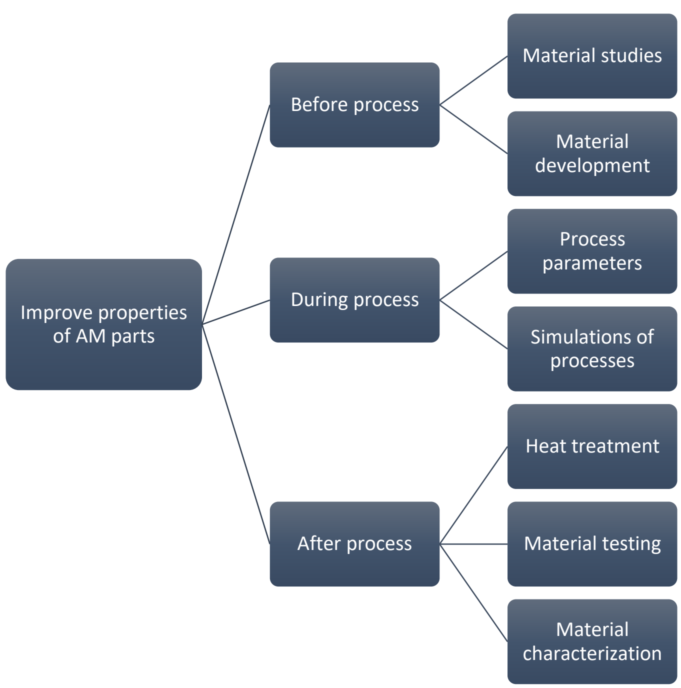

Figure 2.16. Different approaches in additive manufacturing studies

2.6 Previous work on powder characterization

The characterization of metal powders is essential for fully understanding their behaviour. Moreover, it is a critical factor in the development of new materials for powder-based manufacturing.

Common experiments to characterize powders are as follows [61][62]:

- Particle density
- Particle size distribution
- Particle morphology
- Particle crystalline phases
- Particle elemental composition
- Particle chemical composition, and
- Flow characteristics.

Some of the variables listed can be measured using different methods, depending on the expected results and achievable conditions. The American Society for Testing and Materials (ASTM) lists different tests to measure such variables, but in some cases the tests are simply recommendations, offering the possibility of innovating or adjusting them.

In the case of measuring particle density, it is hard to study using traditional methods because of the dimension of the particles. Some methods used displacement of fluids to determine the mass of materials. In the case of powders, a fluid must be used that can access all the particles and their pores. In helium pycnometry, helium is used to fill a receptacle containing a sample. The amount of helium is controlled and measured to determine the true volume of the particles.

To determine the size of the particle, different methods are recommended. Using the B214 test method from ASTM, sieves ranging from 45 to 100 μm are used to determine the sizes of different particles. However, this method is not recommended for smaller particles. The B822 test method uses light scattering to determine particle size distribution. Finally, image analysis methods are also acceptable, but they are not standardized for this purpose [62].

The ASTM standards indicate that there is no standardized method to quantify the morphology of particles, but they claim that the morphology can be determined using image analysis and light scattering [62].

To determine the elemental composition of a powder, different methods can also be used that are very specific to the materials because of their different reactions. But there are also more general methods such as X-ray fluorescence or optical emissions spectroscopy.

Other standardized methods are capable of measuring the flowability of moving powders. Such methods are generally measuring the amount of mass or volume moving during a given time. Powders with different characteristics, such as variable particle size and irregularly shaped particles, will yield inconsistent results. For such circumstances, other nonstandard and more specialized methods are suggested.

In the case of thermal conductivity, there is not a definitive method listed. The ASTM standards do not provide recommended methods to measure thermal conductivity, but they do mention the hot plate method in a general list of methods in use.

2.6.1 Methods to measure thermal conductivity in powders

Three are two principal approaches to analyse thermal conductivity: steady state and transient state, their own advantages and limitations. Therefore, experimental setups are designed to fit certain conditions and objectives.

In general, steady-state methods measure the difference in temperature (ΔT) caused by heat flow (Q). To generate heat flow, a heat source and a heat sink are needed.

The disadvantages of the steady-state methods are as follows:

- Heat loss
- Contact resistance of sensors, and
- Long time to reach the steady-state temperature gradient.

In transient-state studies, temperature changes are applied periodically or as a pulse, providing control to conduct measurements for every established period. For that reason, transient experiments are faster to perform.

2.6.1a Hot plate method

The hot plate method is used to measure thermal conductivity in materials that have low thermal conductivity or insulation properties. The hot plate method is a stead-state method that consists of placing a sample between a heat source and a heat absorber. Like other methods, imperfections in the design lead to corrections being applied to the results using theoretical analysis [63]. Figure 2.17 shows the basic concept. The hot plate consists of different heaters, which are usually electrical resistant, while the cold plate is a block with cooling channels. At least one pair of sensors, mainly thermocouples, are used to measure the gradient in temperature across the sample. Because the heat flux is controlled, and the difference between T_1 and T_2 is known, no other variables are measured to calculate thermal conductivity using a one-dimensional equation.

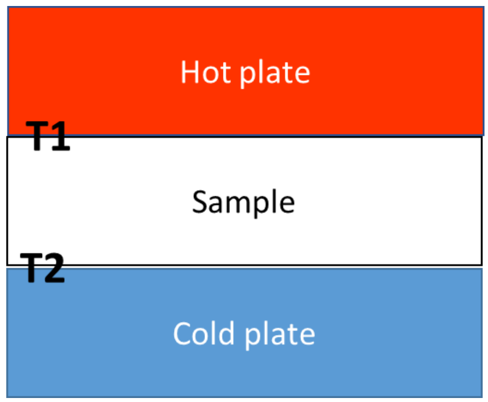

Figure 2.17. Basic concept of the hot plate method.

2.6.1b Transient plane source method

This method uses a plate that can be electrically heated, and two samples are positioned on either side of the plate (Figure 2.18). Applying a constant current, the temperature of the disk increases, but the current also affects the temperature of the samples themselves. The temperature of the samples must be monitored at constant intervals of time. For that reason, proper instrumentation is required; it consists of adding sensors that have the sensitivity to detect changes in temperature in a short amount of time. Therefore, the increase in temperature is a function of time.

The transient plane source method has shown great accuracy for temperatures up to 500K for both liquids and solids. However, its accuracy decreases when it is used for powders or granular arrangements because the contact region is not constant between the plate and the particles [64].

Other sources of errors are as follows [65]:

- Thermal contact resistance between testing samples and sensor
- Thermal inertia of the sensor
- Heat capacity of the electrical isolation elements, and

- Electrical resistance changes with temperature in the disks.

A general analytical model can be adapted depending on the experimental setup:

$$\Delta T(\tau) = \left[\frac{Q^2 V_1 V_2}{(V1+V2)^2 R_{e,s}} - \frac{C\Delta T(t)}{t}\right]\frac{D(\phi)}{\pi^{1.5} r k} \quad \text{Eq. 2.1}$$

where $\phi = \sqrt{t\alpha/r^2}$ in a transient plane

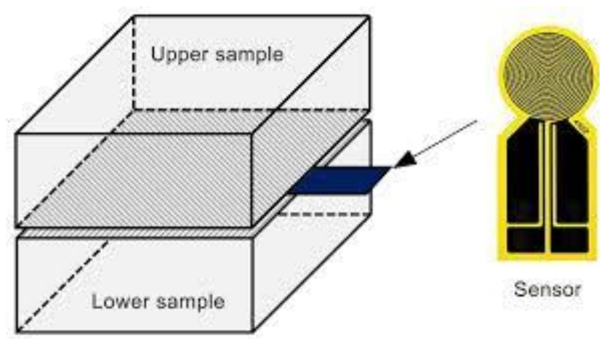

Figure 2.18. Principal parts of the transient plane source method [64].

2.6.1c Hot wire method

The hot wire method is a technique that uses a linear heat source to create a heat flux through a sample (Figure 2.19). As the heat source is operating, the heat spreads in multiple directions, but it can be measured in one dimension because of the radial temperature. The applications of the technique are usually restricted to liquids, but it can also be used with powders. The hot wire method is a transient method, and for that reason, the equations are time dependent [65].

The hot wire method can also be used to measure thermal conductivity under different conditions. For instance, experimental setups are developed to measure thermal conductivity under different gas atmospheres and pressures. Therefore, the effective thermal conductivity of powders can be measured under a variety of conditions [66].

$$k = \frac{p}{4\pi[T(t_2) - T(t_1)]L} ln\left(\frac{t_2}{t_1}\right) \quad \text{Eq. 2.2}$$

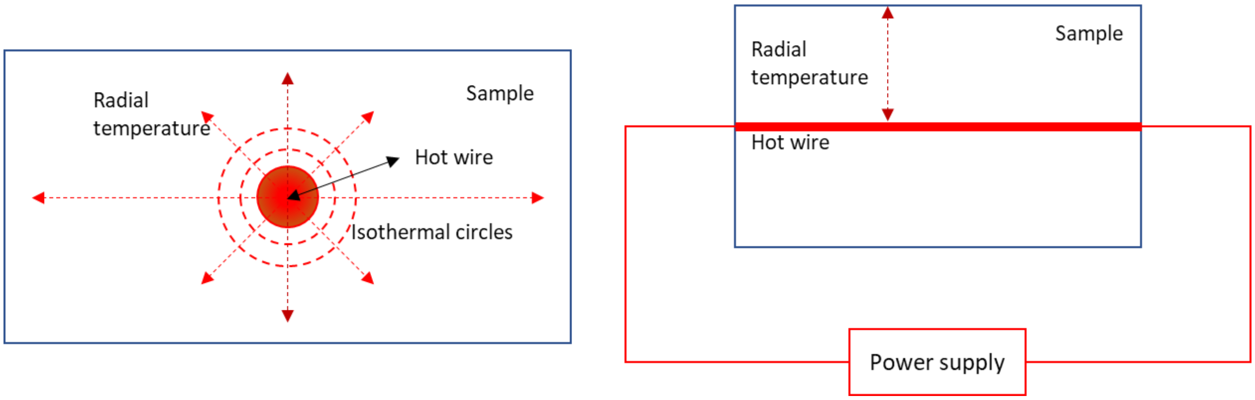

Figure 2.19. Hot wire method.

2.6.2 Analytical approximations of thermal conductivity

Many attempts have been made to calculate thermal conductivity in powders. The complexity of the problem stems from the number of factors that are inherent to the powder beds. First, the particles of powder are not perfectly spherical, causing variations in contact areas. Second, the size of the powder varies within an acceptable range; therefore, the complexity of a perfect analytical solution increases. Finally, the spatial arrangements of the powder must be predicted.

Some researchers have been working on developing models to simplify these calculations. Such models make the problem easier by making a series of assumptions: assuming that all the particles have the same size; assuming that the particles are completely spherical; or supposing that all the particles follow a strict spatial arrangement. At the end, such assumptions have been accepted because of the similarities between theoretical results and experimental results.

The morphology of the powder presents an important challenge in analytical models, as the area involving the conduction mechanism of the particles is much smaller than the area interacting by convection [67]. For that reason, the concept of effective thermal conductivity is used. Effective thermal conductivity does not isolate the particles completely but includes the interaction for convection, resulting in a combined thermal conductivity.

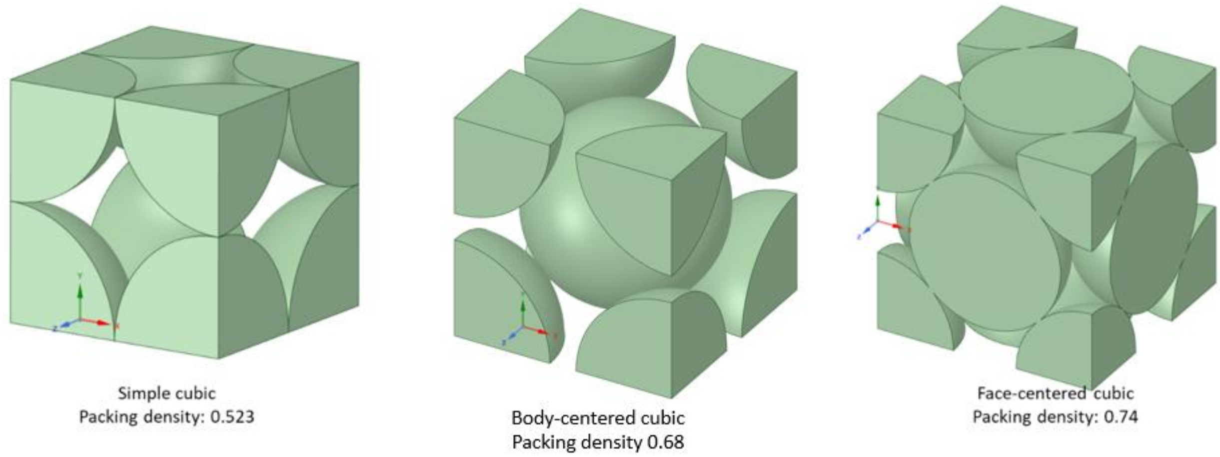

Figure 2.20. illustrates how the particles are arranged in these cubic structures and their total

To represent a powder's structure, the particle arrangements are simplified to define the points of contact and its relative density or packing density. Cubic representations of a unit cell show how the spherical particles are arranged. The most common cubic representations are the simple cubic (SC), face-centered cube (FCC), body-centered cube (BCC), and diamond-like.

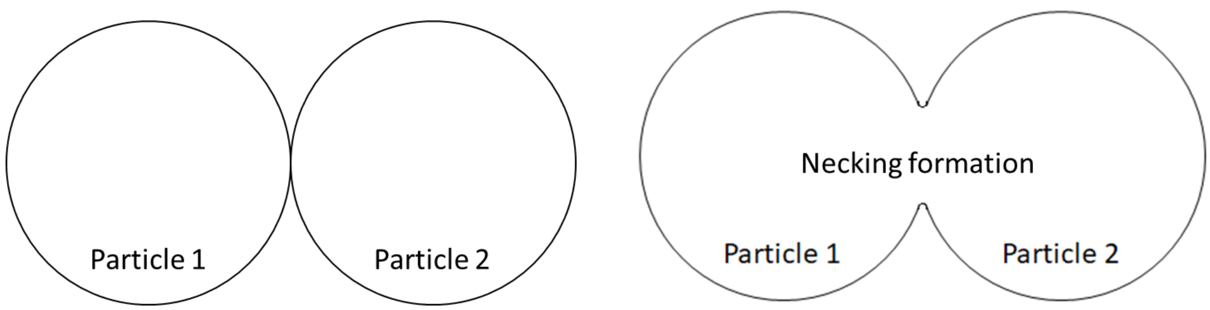

Figure 2.21. Particles before and after receiving enough heat to sinter.

Heat transfer is affected by the fusion between particles as the thermal contact points increase (Figure 2.21). Different powder dispersions also affect thermal conductivity because the number of contact points varies in the different arrangements [68]. In the study of heat transfer in spherical particles, the temperature is considered a scalar, and the direction of transmission is perpendicular to the contact point between them (Figure 2.22). For that reason, the heat flux vector changes according to the different packing structures.

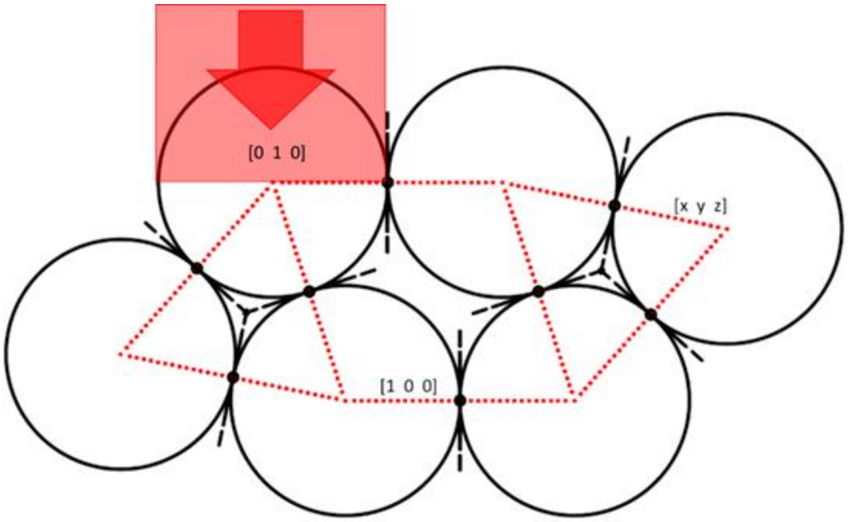

Figure 2.22. Random two-dimensional powder arrangement indicating the heat flux interaction between particles.

The following equations are analytical models developed according to different variables and needs. They follow different considerations and show different applications. The accuracy of the model depends on certain conditions being met. Initial models were not considered to be used specifically in powder beds, but later studies related to their application to the field.

2.6.2a Maxwell equation

In 1873, Maxwell modeled the thermal conductivity of particles in a matrix [67]. However, the model did not fully cover the influence of the dispersed particles when $f_s \rightarrow 0$:

$$\frac{\lambda_e}{\lambda_g} = \left(1 - 2f_s \frac{1-\lambda_s/\lambda_g}{2+\lambda_s/\lambda_g}\right) \Big/ \left(1 - f_s \frac{1-\lambda_s/\lambda_g}{2+\lambda_s/\lambda_g}\right) \qquad \text{Eq. 2.3}$$

2.6.2b Bruggeman equation

Bruggeman attempted to improve the work of Maxwell, changing the matrix to have a homogeneous environment influenced by close particles [67]. Recent studies have shown the accuracy of the model when the volume fraction $f_s < 0.2$, which is value much smaller than the packing of powder beds [67]:

$$1 - f_s = \frac{\lambda_s - \lambda_e}{\lambda_s - \lambda_g} \left(\frac{\lambda_g}{\lambda_e}\right)^{1/3} \qquad \text{Eq. 2.4}$$

2.6.2c Reimann–Weber equation

The following equation considers a constant SC structure; therefore, the relative density is fixed. Another important variable of the model is the contact size ratio, which is calculated with the contact radius and the particle radius [68]. This ratio is also used in other methods:

$$\lambda_e = \lambda \left(\frac{1}{x} + \frac{1}{\pi} ln \frac{2}{x}\right)^{-1} \qquad \textit{Eq. 2.5}$$

Where:

$$x = \frac{r_c}{r_p} \qquad \textit{Eq. 2.6}$$

2.6.2d Equation for random particle structure

In contrast to other models the following model is used to calculate the thermal conductivity of random structures. An assumption made when using the model is that there is a constant number of contact points. One other consideration is that the value of the contact size ratio should be within a defined range of effective thermal distribution structure ($0 < x < 0.3$) [68]:

$$\frac{\lambda_e}{\lambda} = \frac{\rho\, n}{\pi}\, x \qquad \textit{Eq. 2.7}$$

2.6.2e Heat flux density–based equation

A different approach was followed to calculate effective thermal conductivity. Because it can be detected, the model can be assumed to be general for the different particle distributions and densities. Even more, the variables used in the equation seem to be more suitable for experimental determination, so it is not a completely analytical solution. The following equations are derived by the heat flux density [68]:

$$\varphi = \frac{F}{A} = \frac{\Delta T}{SA} = \lambda_e |\nabla T| \qquad \textit{Eq. 2.8}$$

where thermal resistance of a circular contact is:

$$S = \frac{1}{2\lambda a} \qquad \textit{Eq. 2.9}$$

2.6.2f Limitations of analytical models

As stated earlier, no single equation can take into account all the variables involved in the real interaction of particles. The nature of the process is full of imperfections that challenge standard methodologies. Therefore, it is important to discuss the following points:

- Dependence on gas pressure. Studies have revealed that effective thermal conductivity is affected not only by the type of gas used in the process but also the pressure of the gas. Higher gas pressure increases density and thermal conductivity [66][67].
- Gas particles. Despite the differences in thermal conductivity among noble gases, experiments shown that the atomic size of gases also affect thermal conductivity [67]. Consequently, experiments on effective thermal conductivity should be performed under different atmospheres.
- Powder particularities. Real powder particles are not perfect. The size of the particles is not constant, and their arrangement does not perfectly follow a pattern. For that reason, expecting an absolute analytical result is not feasible, and some geometric assumptions are normally considered in most models [67].

2.7 Conclusion

AM applications are growing in popularity, demanding more reliable parts. Nowadays, there are different approaches to predicting and improving material properties, but different types of imperfections continue to affect the final properties of 3D printed parts. Therefore, more studies should be done to reduce the risk of failure in parts.

Powder particles that do not fuse correctly can generate faulty manufactured parts. As a result, how particles join and interact should be better understood. However, studies of metal powders are not completely standardized owing to the large number of parameters and the many differences in materials and machines. Despite some recommendations from the ASTM, there is no standard experimental method to calculate thermal conductivity. Finally, while using analytical methods can produce reasonable approximations and estimates of thermal conductivity, the results are not completely accurate because of the many factors related to the imperfections of the powder.

Chapter Three: Study of thermal conductivity of stainless steel 316L powdered

According with the conclusion from the previous chapter, additional experiments were needed to investigate the thermal conductivity of powdered materials. Mathematical models are limited to a number of parameters that are not constant under real conditions. Therefore, it is important to compare experimental and theoretical results. In this chapter, the results of these experiments are presented. Using a tubular furnace, thermal conductivity of the powder was measured when the powder was exposed to temperatures in increments of 100°C. Variation in thermal conductivity is expected for powders with different structures. The challenges of the experiments are attributed to the powder's particle size and imperfections.

3.1 Introduction

Additive manufacturing (AM), or 3D printing, has been gaining in popularity across diverse sectors in recent decades [1]. As a result, AM equipment has become more affordable and accessible. Polymers are the most popular materials to use in AM, and a large community is dedicated to developing materials, models, and process optimizations [69]. Metallic materials for AM are still in development, as many metals cannot be used owing to their inadequate solidification [69]. The cost of metallic AM is still considered high, including the cost of fabricating the final parts themselves as well as purchasing the equipment and materials. Some of the industrial limitations can be attributed to the complexity of the systems, such as the limited number of materials available. Others are occasioned by the AM concept, like slow mass-scale production or challenges with the properties of the materials.

AM uses different processes to print metallic materials. Some of the most popular are based on powder bed fusion (PBF). All PBF processes share the same elements: they require at least one heat source (laser or electron beam), a movement controller for the heat source, and a system to control the powder's layers (Figure 3.1) [70].

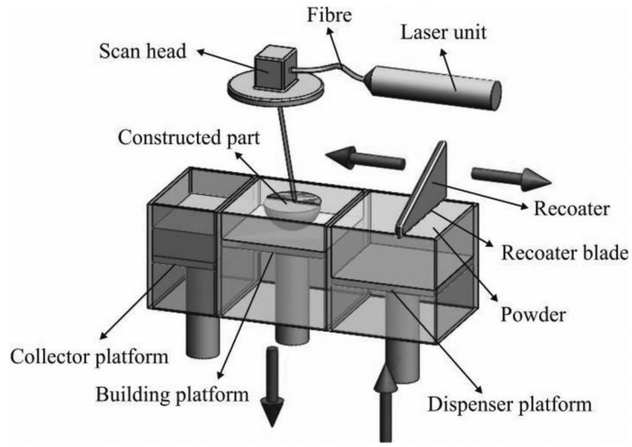

Figure 3.1. Example of the components of a DMLS system [71].

Some manufacturers use a roller or a blade to add more powder. EOS Gmbh, for instance, uses a hard-recoating technology to achieve a higher density. The coating blade is intended to be harder than the material processed to avoid contamination. However, compared with soft recoating systems, some shear forces can be generated by hard recoating blades; hence, there is a risk that the printing process can fail [72].

When the laser is melting the material, the effects caused in the powder are complex due to the high thermal gradients in the particles. As a result, the material will expand and contract in different directions, leading to a common problem called residual stress [72].

Other problems that arise during the 3D printing process are attributed to the lack of melted material. When the laser spot contacts the powder bed, some quantity of material is vaporized because of the large amount of energy coming from the laser. Moreover, the laser energy throws powder particles out of the path. Hence, the total material available to be melted decreases, increasing the porosity of the final part [7].

In this part of the study, properties of the raw powder were characterized with the goal to improve the final properties of the printed parts. Thermal conductivity is an important factor to understand the thermal gradients present in the material. One reason is that thermal conductivity is a parameter that increases with temperature; thus, knowing its behavior at sintering temperatures will help to yield more accurate models. As a result, optimizing thermal conductivity can help to improve the final properties of the printed parts.

There is no formal standard for measuring the thermal conductivity of powders. However, the ASTM has proposed the thermal hot plate method as one approach [62]. Unfortunately, the setup of the hot plate limits the maximum temperature that can be reached. The higher the temperature, the more complicated it is to have a safe apparatus because of the heat resistance of the elements. In contrast, tubular furnaces can safely reach more than 1000°C, which is more suitable for the intended purpose. Furthermore, the cylindrical shape has the advantage of not experiencing heat loss [73]. Finally, tubular furnaces are suitable for use in inert atmospheres and vacuums.

The principal purpose of this experiment was to determine the effective thermal conductivity of the selected powder. In order to obtain this value, it must be understood that thermal conductivity changes with temperature. Therefore, in order to have more control of the printing process, the incremental change in thermal conductivity within different temperature ranges must be determined. Consequently, future analyses of experimentally determined thermal conductivity data will be assumed to relate only to certain powder bed conditions. Moreover, creating different powder densities offers more opportunities to recreate processes and achieve more accurate results to be used in simulation studies.

3.2 Methodology

It is challenging to measure the thermal conductivity of a single powder particle with a size of ~50 µm because of the physical limitations of available equipment. Further, the interaction of a single powder particle with neighboring particles makes it more challenging to determine the effective thermal conductivity between powder particles. The variation in the radius and porosity of a given powder also generates many different configurations, changing the contact area between particles. Therefore, the following experiment is not limited to measuring the thermal conductivity of an isolated sphere.

To accomplish the objective of determining the thermal conductivity of the powder, a method needed to be developed that could be adapted for use with different particle densities but also at high temperatures, at least up to the sintering point of the powder. Therefore, the heating equipment must be able to safely reach a high temperature. In addition, the sample should be independent from the system, meaning that the sample can be changed and varied without major operational changes. Finally, the instruments should be located at the correct points to obtain the most accurate results possible from the experiment.

The apparatus used for this experiment was a model EHA 12/450B tubular furnace manufactured by Carbolite Gero Ltd., used with a EUROTHERM 3216 PID controller. The maximum temperature that can be reached with this equipment is 1200°C, which is an adequate temperature given the sintering point of stainless steel. An important consideration when using the furnace is that the ramping rate is limited to 5°C/min, which is more suitable for steady-state experiments, but the action response of the system is not adequate to generate and detect data for a transient analysis.

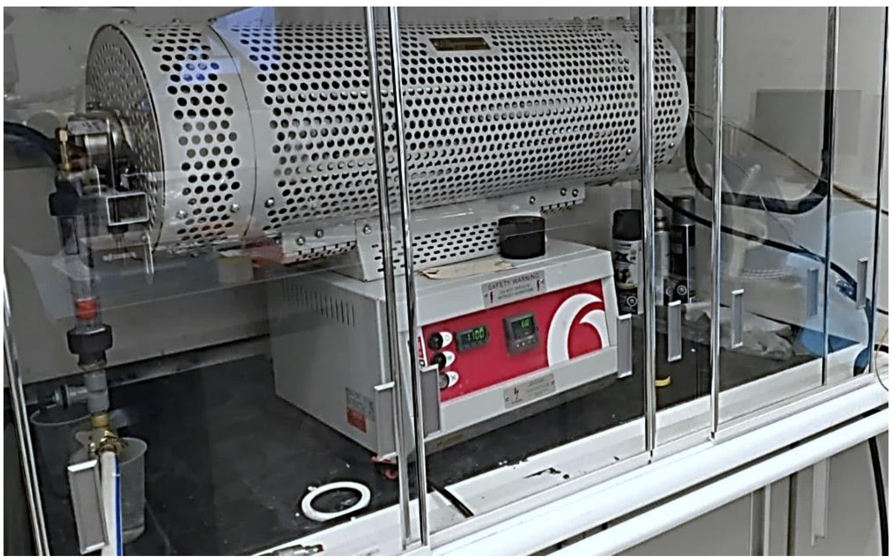

Figure 3.2. Experimental setup featuring the model EHA 12/450B tubular furnace made by Carbolite Gero.

The powder used for the experiment was manufactured by EOS GmbH under the name EOS Stainless Steel 316L. Commercialized powder employed in the experiment was certified using ASTM B214 getting a particle size distribution of 20-65 μm [74]. EOS Canada claims that the 316L class of stainless steel is appropriate for a large number of fields, including automotive, aerospace, jewelry, food and chemical plants, and medicine. Some of the properties that they highlight includes the material’s corrosion resistance, ductility, opportunity for postprocessing, and its potential utilization in surgical implants [74].

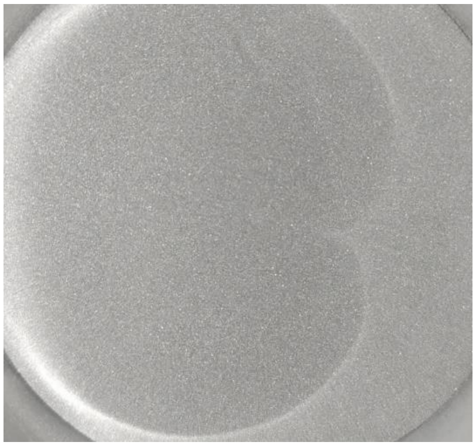

Figure 3.3. Example of stainless steel 316L powder used for the thermal conductivity experiment.

The recording of the temperature was performed using an OMEGA HH506RA thermocouple data logger with type-K model OMEGACLAD XL thermocouples connected; Figure 3.4 shows thermocouples 1 and 2. The data were transferred directly to the computer in steps of 3 s. In addition, a second pair of thermocouples was added to monitor the temperature of the water.

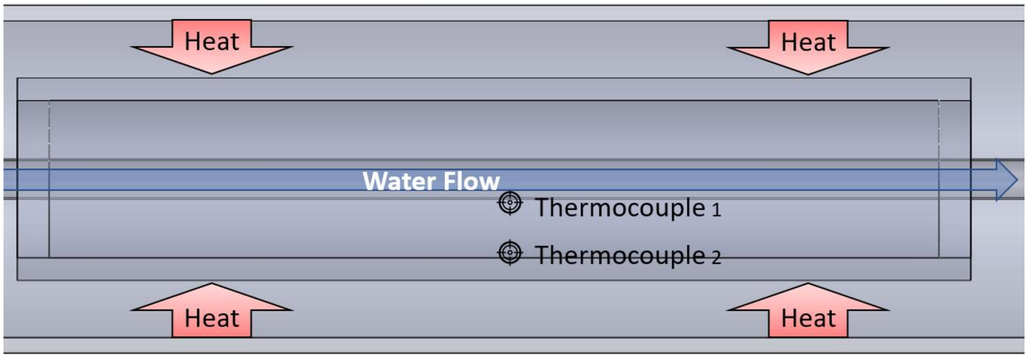

Figure 3.4. Experimental setup showing the position of thermocouples 1 and 2 in the sample inside the tubular furnace. Thermocouples A and B are located at extreme ends of the system.

The following experiments were performed to achieve two goals while identifying the differences in thermal conductivity using different methods. The first goal was to magnify the importance of the preheating process. The second was to test thermal conductivity when the temperature of the material reached the sintering point, at which point the particles start to consolidate. Reaching the melting point of the material was not part of the experiment, as the portion of the sample being measured would change drastically; therefore, the measurements would not be accurate.

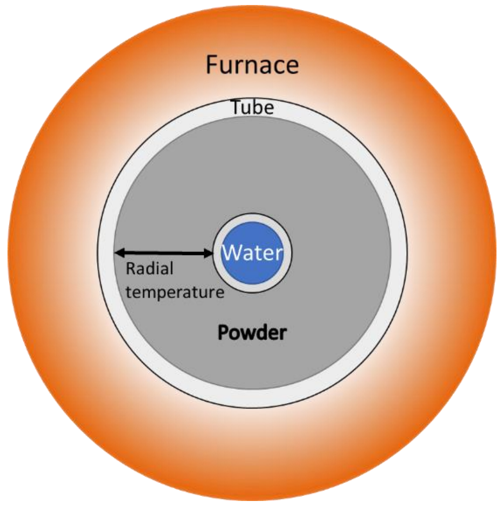

Figure 3.5. Cross-section of the experimental setup. The thermocouples measure the gradient of the radial temperature in the sample.

The container holding the powder was a stainless-steel tube that was placed in the center of the tubular furnace. In order to achieve a uniform heat distribution, the powder sample was placed in a ceramic support that covered only a small part of the surface at the bottom.

The powder was prepared using three different methods. For the first sample, powder alone was deposited without external factors; that is, the powder was deposited by gravity. For the second sample, the powder was compressed 10% of its original size. The third sample was filled by attaching vibration elements to the container. Better thermal conductivity was expected when testing the compressed sample.

The experiment captures the changes in gradients of temperature every 100°C, starting at 100°C and ending at 1000°C. After reaching the study temperature in the furnace, the temperature was held to achieve a steady state in the system. For that steady state, the gradient of temperature in the water between thermocouples 1 and 2 was measured. Using those values, it is possible to calculate the heat flux in the system using Eq. 3.1 [75]:

$$q = kS\frac{\Delta T}{L} \qquad \text{Eq. 3.1}$$

However, the shape of the surface used in contact is a cylinder, so the equation must be adjusted to accommodate this geometry [76]:

$$q = \frac{2\,\pi\,k\,\Delta T}{2.3\,log\frac{r_0}{r_1}} \qquad \text{Eq. 3.2}$$

Therefore, to calculate effective thermal conductivity, the equation is as follows:

$$k = \frac{q\ 2.3\ log\frac{r_0}{r_1}}{2\ \pi\ \ \Delta T} \qquad \textit{Eq. 3.3}$$

To solve Eq. 3.1, the variable *q* of heat flux is unknown, and therefore Eq. 3.4 [77] was selected as a way to calculate this magnitude. Eq. 3.4 determines the heat flux in the system, measuring the change in temperature when a fluid is passed through the system. In the case of this experiment, it is expected that the heat flux must change for all the cases in the different samples:

$$q = \dot{m}\ c_p\ (T_a - T_b) \qquad \textit{Eq. 3.4}$$

The temperature of the water should be monitored to avoid having it reach 100°C, at which point it changes state from liquid to gas. Therefore, the flux of water needs to be fast enough to leave the system in a safe range of temperature. However, to measure the temperature, it is better to ensure laminar flow in the system to reduce the amount of water flow. The Reynolds number determines whether the flow is laminar or turbulent. In this case, it is important to obtain a Reynolds number under 2300 to ensure laminar flow. The Reynolds number is calculated using Eq. 3.5 [77]. Note that some properties of water change with temperature, and this was considered as part of the calculations.

$$Re = \frac{\rho\ V_{avg}\ D}{\mu} = \frac{V_{avg}\ D}{vi} \qquad \textit{Eq. 3.5}$$

3.3 Results

As stated in the Methodology, to determine the thermal conductivity of a powder, the heat flux in the system must be measured. First, the temperature of the water during the steady state remained an almost constant value, as shown in Figure 3.6. When water flow was established at 30LPH to achieve laminar flow, the Reynolds number was 1890, as calculate using Eq. 3.5. The temperature of that segment corresponds to the steady state indicated in Figure 3.7.

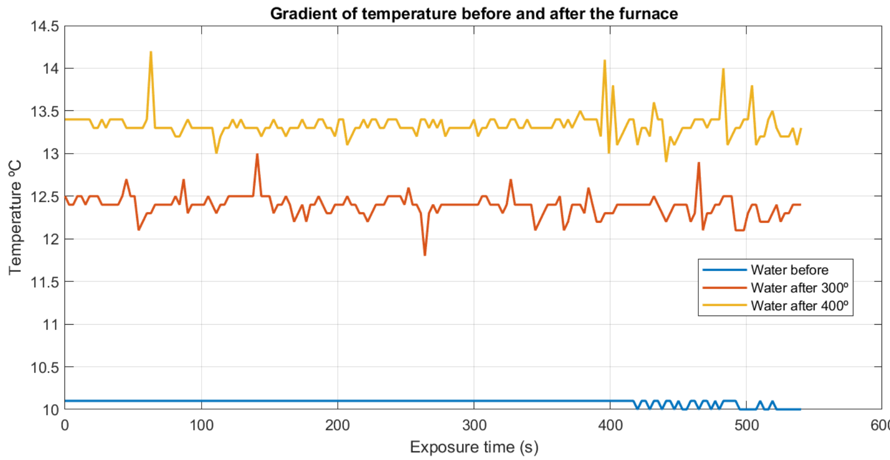

Figure 3.6. Example of water temperature in the system. The water was measured by thermocouples A and B located before and after entering the furnace.

Having the temperature measurements of the water, it was possible to calculate the heat flow absorbed by the system using Eq. 3.4. Figure 3.8 shows the amount of heat moving in the system. The temperature of the water increases as the water passes through the system. Preliminary results can be seen in Figure 3.9, when the gradients of temperature are compared. The compressed powder shows a smaller distribution in temperature.

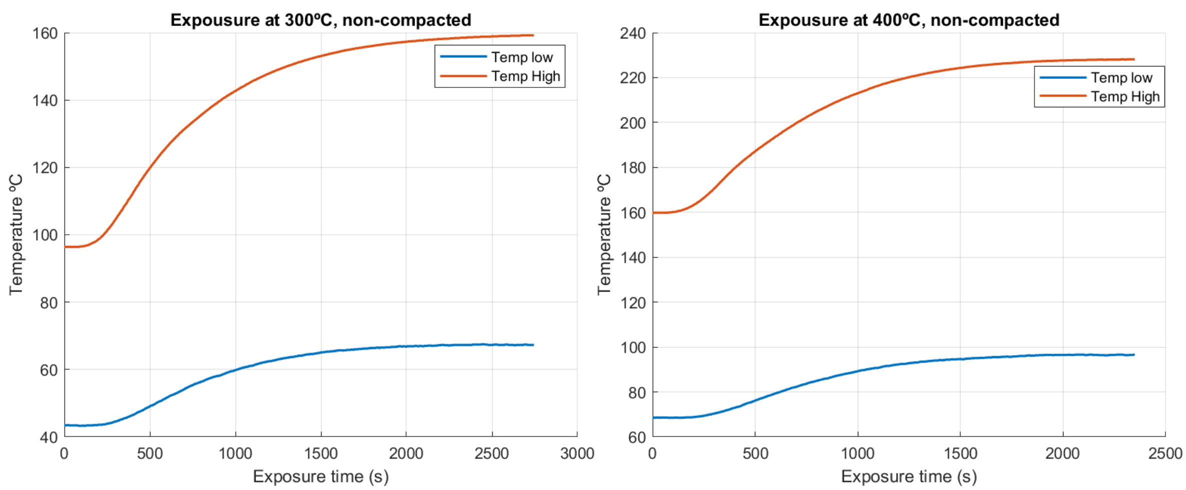

Figure 3.7. Representative results obtained from the powder sample in thermocouples 1 and 2, denoting the data for analysis in a steady state. The left panel shows the increment in the temperature gradient between the thermocouples at 300°C, while the right panel shows the same for the temperature gradient at 400°C.

More heat is absorbed by the system in the noncompacted structure; this is caused by the large gradients of temperature in the sample. General Eq. 3.1 shows that heat flux depends directly on the difference in temperature. In the last two steps of the experiment, an important variation was observed, which might be occasioned by material sintering.

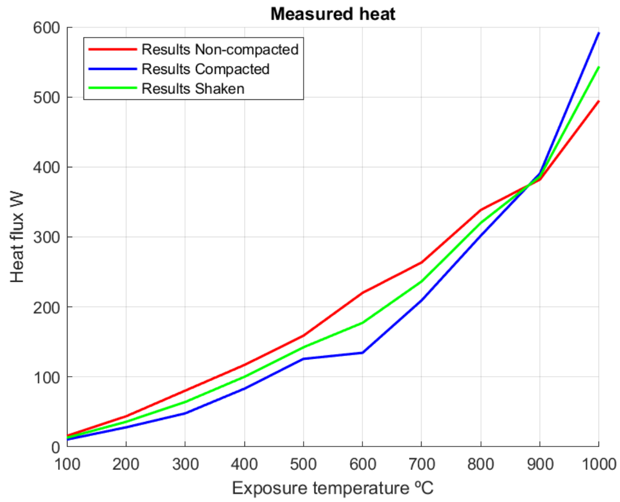

Figure 3.8. Heat flux absorbed by the system at different temperatures.

Testing revealed that the time required for the sample to reach a steady state was usually between 30 min and 1 h, as can be seen in Figure 3.7, which compares the steady state of two principal stages of the experiment. These calculations considered the temperature gradient between the thermocouples in the steady state (Figure 3.9); the changes in temperature that occurred during ramping were not considered in the calculations.

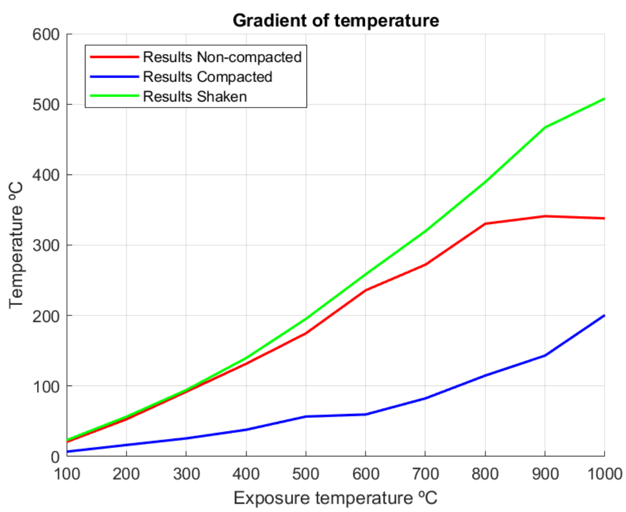

Figure 3.9. Comparing temperature gradients in the steady state at the different stages of the experiment. The temperature in the compacted sample is far lower compared with that of the other samples.

Using the values obtained from these experiments, the calculations of effective thermal conductivity were performed. Figure 3.10 shows the results obtained from the experiments. As can be observed, the thermal conductivity is higher in more compacted or defined structures. In the case of the noncompacted samples, an important increment can be observed in the last step, which came about through auto-compression due to sintering and deformation.

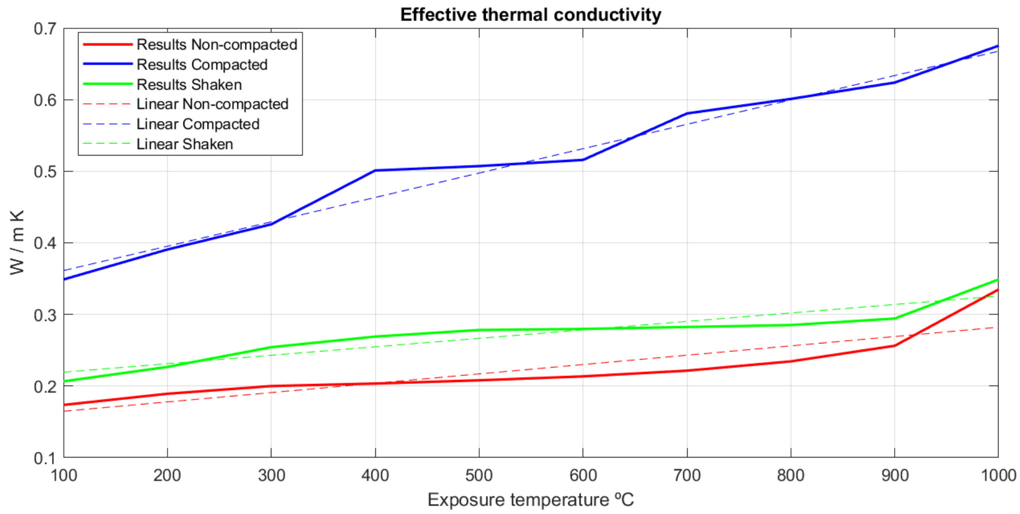

Figure 3.10. Effective thermal conductivity results and linear characterization. Solid lines represent the average obtained from experiments; the noncontinuous line represents the linear relationship.

3.4 Discussion

In the calculations of heat flux, temperature in the water did not increase as drastically as the temperature inside the furnace. The reason is related to the nature of the heat source. The tubular furnace radiates heat to the surface of the tubular container. As a result, the powder sample interacted with two different types of conduction: a conduction flow of water causing convection and radiation emitted from the furnace. Hence, water flow will have a greater impact, as can be seen Figure 3.6.

Suitable analytical methods are also presented to compare the difference between the results obtained. The chosen methods depend on certain limitations and variables. Some consideration must be given to the model representing the powder structures with defined arrangements and contact regions.

The Bruggeman equation (Eq. 3.6) uses the thermal conductivity of the environment, the volume fraction occupied by the powder, and the thermal conductivity of the bulk material [78]. The Reimann–Weber equation (Eq. 3.7) is limited to simple cubic representations, but includes a variable representing the ratio of area in contact with particles [78]. Finally, a third equation (Eq. 3.8) is used for nonconstant arrangements, considering the volume fraction, the ratio of contact area, and the estimated number of contact points in a representative cube [79].

$$1 - f_s = \frac{\lambda_s - \lambda_e}{\lambda_s - \lambda_g}\left(\frac{\lambda_g}{\lambda_e}\right)^{1/3} \qquad \textit{Eq. 3.6}$$

$$\lambda_e = \lambda\left(\frac{1}{x} + \frac{1}{\pi} ln\frac{2}{x}\right)^{-1} \qquad \textit{Eq. 3.7}$$

$$\frac{\lambda_e}{\lambda} = \frac{p\, n}{\pi}\, x \qquad \textit{Eq. 3.8}$$

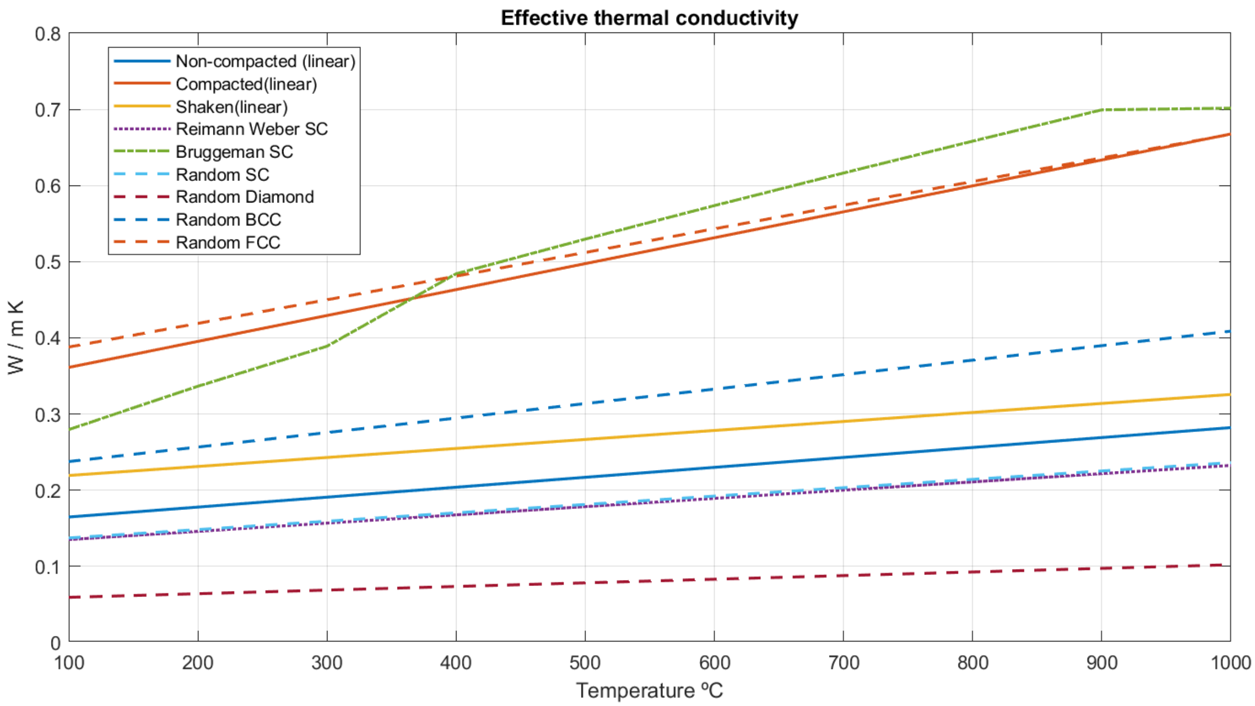

Figure 3.11. Analytical and obtained experimental results of effective thermal conductivity.

After comparing and interpreting the results from the temperature gradients using eq. 3, the assumption can be made that the larger temperature gradient has a significantly lower thermal conductivity. The thermal conductivity was then calculated using Eq. 3.3 and compared with the known values from the literature (Table 1). The calculated thermal conductivity of the powder is only a fraction of the bulk material. Such findings have been attributed to the nature of the samples, as the area of contact and voids between the particles significantly affects thermal conductivity. However, the compressed sample had a higher thermal conductivity.

Finally, after comparing the results from other analytical methods, the noncompacted results were located close to the less compacted diamond structure. While the compacted results are higher than the simple cube (SC) results, they did not reach the values calculated for a body-centered cube (BCC).

Table 3.1. Effective thermal conductivity and thermal conductivity of a solid material.

Stainless steel	**Thermal conductivity (W/m·K)**			
	Bulk material	***Compacted***	***Shaken***	***Noncompacted***
Min. (100°C)	15.87	0.3612	0.2193	0.1736
Max. (1000°C)	27.3	0.6676	0.3257	0.2822

3.5 Conclusion

Using a custom experimental setup, the thermal conductivity of powder samples with different characteristics was measured. Results revealed that structures formed by the powder play an important role in the fusion process. The thermal conductivity of a compacted structure improved dramatically. When the volume of a powder was compacted by 10%, the resulting thermal conductivity almost doubled compared with that of the noncompacted sample. Moreover, compaction has important theoretical benefits that can improve the quality of 3D printed parts.

In terms of comparing the experimental results with previous analytical solutions, these analytical solutions were modeled to be applied to perfect powder structures with constant contact surfaces. Therefore, variations with experimental results WERE expected. Results from the compacted sample are close to the values calculated using the Bruggeman equation after 200°C. However, when comparing with the undefined structural equation, the results almost matched those for the FCC structure.

Additionally, shaking the sample did not generate a significant difference with noncompacted results. In addition, when comparing with the analytical model, the results were located between the range of BCC and SC; for initial conditions, results were closer to BCC, but did not exhibit the same linear incremental rate.

It is important to mention that the equations used here yielded results that were similar to the experimental results. However, some of the models do not consider the thermal conductivity of the atmosphere, a factor that could lead to inaccurate results in the event that the sample was exposed to a different gas.

Finally, these experimental results obtained here are useful for performing AM simulations. The initial value of thermal conductivity can be modified, such that it is adjusted according to other variables. Moreover, thermal conductivity can be treated as a dependent variable in the simulation, to be adjusted to the surrounding temperature of the laser spot. Likewise, optimizing powder structures would be beneficial to reduce fusion problems in the printing process.

Chapter Four: Simulating the Impact of Thermal Conductivity on Powder Bed Processes

In this chapter, simulations of the interaction between the powder material and the laser path are compared. Results from the experiments described in Chapter 3 are used to simulate the effect of thermal conductivity on powder beds. Simulations were performed in a model at scale, with the principal disadvantage being that there was more information to process. The simulation results' demonstrate that the powder bed has better thermal distribution as thermal conductivity increases.

4.1 Introduction

Additive manufacturing (AM) involves building parts by laying down and fusing together thin layers of material. In the case of powder bed fusion (PBF), each new layer is added on top of the previous layers in a horizontal orientation. AM has important capabilities that allow a user to optimize different parameters of a part. However, the time to produce a component by AM is far longer compared with other traditional manufacturing methods. Production time can be an important limitation, but where feasible, AM can be used in industries where high precision, customizability of parts, and low-volume production are more important.

Recently, more different industries have become interested in the on-demand production of parts with special features. For that reason, they are investing in the development as well as the certification and testing of various production methods. In some industries, certain properties must be achieved to assure the customer of the quality of the part. However, current testing ASTM and ISO standards are not adequate to test all the parts produced by AM [80]. Furthermore, printing parameters have a significant impact on the properties of the final printed parts, including the thermal history of the parts, leading to the fabrication of parts with different microstructures and other undesirable variations. As a result, the mechanical properties of the printed parts are not constant and may vary enormously when comparing different process parameters or even different manufacturers [81][82].

Simulations of AM methods are becoming increasingly accurate owing to the ability to validate models using experimental data. There are several different approaches to simulations. One factor in the selection of the type of simulation is its scalability and computational cost [83].

In order to simulate the laser path involved in fabricating the complete printed part, a large number of iterations are required, which drastically increases the amount of information to be processed. The ideal approach is a simulation representative of a section of the process, thereby greatly reducing computational cost [84].

One approach involves the characterization of powder dynamics through the use of discrete element methods, which follow Newton's equations to simulate the motion of the particles [85]. Motion simulations predict the dispersion of powder when a blade or roller adds a layer of material by considering parameters such as feeder speed, layer thickness, and distribution of powder size [85],[86]. In the case of powder particles that are not spherical, the multi-sphere method joins spheres of different sizes to yield a non-spherical shape [85][86]. However, such methods are still in development for application in thermal simulations.

The accuracy of predicting final properties of 3D printed parts using printing parameters is increasing. Different models have also been designed to simulate the internal granular structure of the printing process [87]. For instance, the Monte Carlo model can predict the microstructure, simulating solidification and grain evolution.

However, simulations of the printing process are also limited to user controls. There are more opportunities to improve the simulations by changing more than operational parameters. Tested and verified models can be used to evaluate modifications in the material values to yield better theoretical final properties, which can be obtained with future changes in the printing process.

One of the essential parameters involved in the process is heat power. Low heat will result in a partial melting of particles, occasioning voids and thus increasing porosity. On the other hand, an excessive amount of heat will vaporize the material and subject the part to extreme gradients of temperature [88]. Therefore, the material should be exposed to an equilibrated amount of heat to prevent major defects.

For this study, thermal conductivity is the parameter that will be modified to obtain different rates of thermal distribution, altering the melting pool. The effects of thermal conductivity and the melting pool will also be studied in more than a single track in order to show the interactions with other laser tracks.

4.2 Methodology

The simulations were performed using one of the most recent compatible versions of software, linking Abaqus CAE v2019 with Intel Parallel Studio XE 2019 Update 5, and Visual Studio 2019 to run coded subroutines. The hardware used was an Intel i7-8700 processor at 3.2 GHz, with 16 GB of RAM DDR4 at 2666 MHz, running single core parallel simulations. It took around 12 hours to run the complete model for the longest case of 2000 steps and 75000 elements, with the advantage that two simulations could be run at the same time.

Abaqus is a software that has predefined configurations to simulate common analyses. However, for some studies it is more complicated mimic physical phenomena. In order to perform such analyses, subroutines are used. Subroutines offer enough flexibility that software limitations can be overcome, increasing the possibilities to the user. They are usually written in a programming language like C, C++, or Fortran. However, subroutines also have their own limitations: the software is limited to reading just one file, but it can include more than one subroutine; subroutines are not capable of calling other subroutines; in some specific cases, subroutines are not able to call utilities in Abaqus [89].

For this study, the subroutines were written in Fortran, a programming language commonly used for numeric and scientific computing [90]. Developed by IBM in the 1950s, FORTRAN is a portmanteau of the words “formula translation.” The applications of FORTRAN are still relevant today, not only for solving problems but also for benchmarking systems. Examples of its uses include finite element analysis, computational fluid dynamics, physics, chemistry, and more [91].

Two subroutines were used for the simulations in the current study: DFLUX and FILM, Appendix A. The DFLUX subroutine is widely used in AM and also in welding. DFLUX is mainly used to simulate a non-uniform distributed flux that can change with different variables (e.g., time or position) [92]. The FILM subroutine allows the user to add the condition of sink temperature for heat transfer analysis [93].

4.2.1 Representative model

In order to simulate powder bed processes, it is usually recommended to use volumetric representations in order to reduce the number of nodes and elements in the model. Such representational models vary in their properties when they are compared with bulk materials because of the presence of voids in the final part.

For the following simulations, the parameter studied was thermal conductivity. Thermal conductivity is greatly affected by the transmission of heat in a combination of mechanisms. The propagation area is significantly reduced to limited contact points between particles, and the rest of the heat transfer occurs mainly through convection, and in smaller proportions: radiation.

To simulate a powder bed, the original shape of the model needed to be represented in order to compare the results. The spheres would be meshed; therefore, the division of the spheres led to a larger number of elements, producing a greater computational cost. Another approach uses the discrete element method (DEM) instead of finite element analysis (FEA), but the results for heat transfer are not consolidated owing to its inaccuracy when heat transfer spheres is studied [94].

Moreover, simulating fixed powder structures in FEA would entail an enormous challenge because of the need to recreate radiation and convection between the voids. In addition, the use of a fixed structure would not be adequate for recreating a real powder bed. Finally, the possible results are not expected to show a meaningful value when comparing with the resources used.

A common analysis of heat transfer in powder beds is limited to a single laser track. It is believed that a single track is representative of all the paths followed. However, it is also important to consider the interaction in the thermal dispersion when a second laser track is involved. In the printing process, the laser spot partially passes for the same laser path. Overlapping allows the new paths of material being attached to the building part, new material and the immediate next and lower layer create a stronger bond.

Previous research has shown the formation of a melting pool when the single track of a laser comes into contact with the powder material [95]. However, after the first melted line, neighbouring regions of the powder bed are drastically heated. Therefore, following the existing tracks in the same layer can melt the powder using less energy.

There are different ways to define the shape of a heat source in a planar surface. If one further considers a third dimension, the model should consider the behaviour of the laser under the surface layer. However, for AM simulations, the study usually includes the interaction with a moving heat source, and therefore the model should be changed from a punctual load to a moving distribution.

Numerous experimental studies have characterized the impact of a laser in powder beds. When a laser is being used, recent research has shown the presence of depression zone, or a keyhole, in the exact same location as the laser spot; this is later followed by the formation of a melting pool. However, the purpose of the present simulation model is not to represent the physical changes in the material but rather its thermal behaviour.

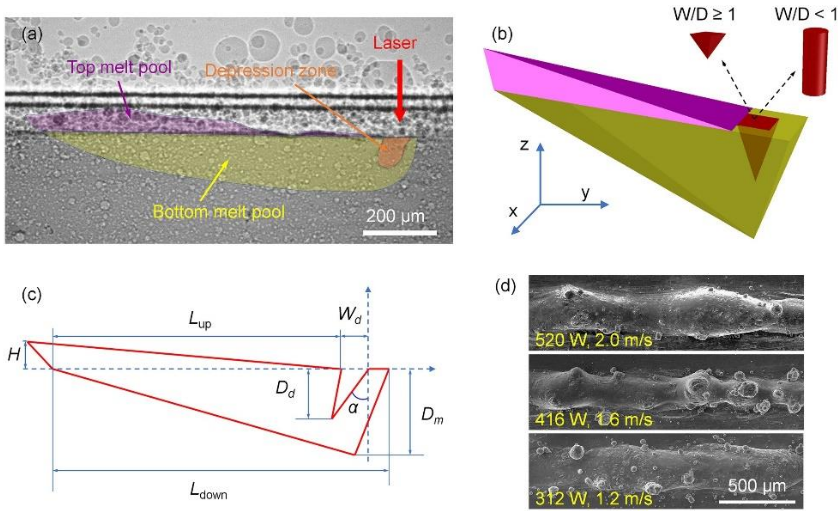

Figure 4.1. Melt pool characterization. (a) X-ray picture showing the regions and their names. (b) Simplified 3D version of the model. (c) 2D representation. (d) SEM examples of top views of laser tracks using the same energy density [96].

The laser model used is the Goldak configuration, a laser profile that is commonly used to simulate laser and welding methods [97], [98]. As was observed when comparing Figure 4.1 and Figure 4.2, the sectional distribution of the laser in the powder bed follows a similar profile.

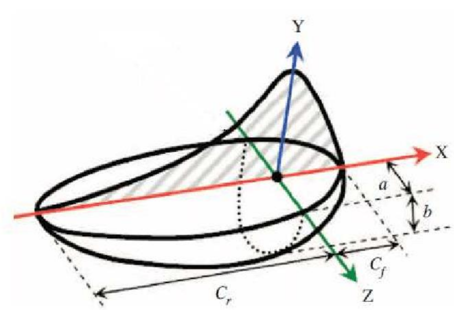

Figure 4.2. Laser characterization showing the heat distribution. It is composed of an arrangement of two circumferences projected in two different planes [98].

4.2.2 Finite element model

The part of the powder bed to be simulated was defined based on a real scenario of a body with a length of 10 mm, a width of 1 mm, and a height of 0.06 mm. The mesh size is 20 μm using DC3D8 elements. The dimensions of the part are an acceptable representation owing to the laser spot having a dimension of 100 μm. The time steps were fixed, but the total time of the simulation changed depending on the scanning speed, which can reduce or increment the number of steps.

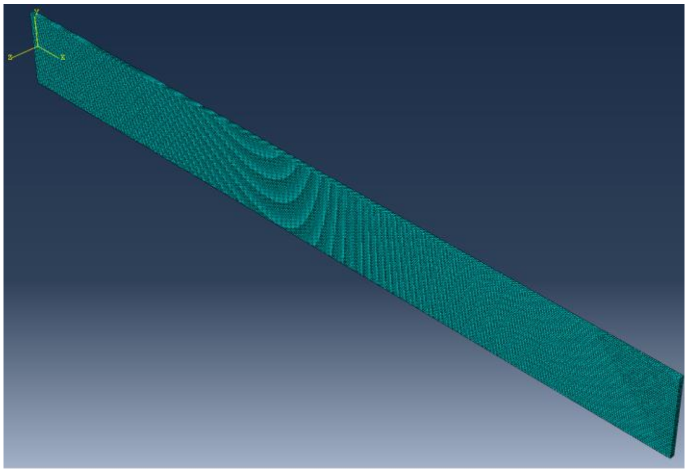

Figure 4.3. 3D part with mesh.

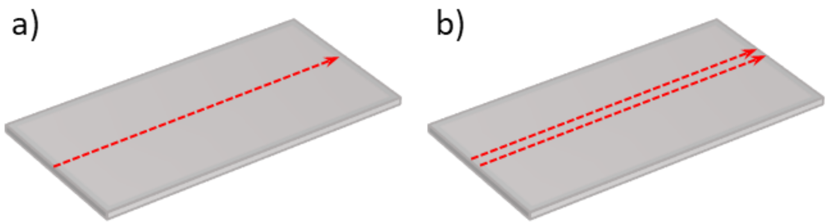

Figure 4.4. Representation of laser tracks for the simulation. (a) First analysis considering a single track. (b) Second study, showing a parallel track in the same direction.

The scope of the study needed to be limited in order to focus on the objective of finding the effect of improving thermal conductivity in powder beds. Therefore, the following assumptions were made:

- The powder bed was considered uniform, with a fixed height, constant thermal properties, fixed particle distribution, and fixed packing density.
- Multiphase effects were not considered.
- Material vaporization was not considered.

- The second track was assumed to be parallel and running in the same direction as the first track; different thermal distributions were possible with other configurations.
- The analysis considered the middle of the printed part in order to collect more information on the thermal distribution in the powder bed; the thermal distribution can also propagate with time.

For the case of the thermal conductivity of the powder bed, different models were compared using the results from the analytical and experimental methods.

Table 4.1. Thermal conductivity data used in the analysis.

Temperature (K)	Thermal conductivity (W/m·K)		
	Gravity (linear)	Compacted (linear)	Shaken (linear)
373	0.165	0.361	0.219
473	0.178	0.395	0.231
573	0.191	0.429	0.243
673	0.204	0.463	0.255
773	0.217	0.497	0.267
873	0.230	0.531	0.278
973	0.243	0.566	0.290
1073	0.256	0.600	0.302
1173	0.269	0.634	0.314
1273	0.282	0.668	0.326

Note: For higher temperatures, software extrapolated the values.

Operational parameters were selected based on the real operation of an EOS GmbH model M280 3D printer and its updated model, M290 [99][95][74]. Table 4.2 shows the parameter range of the machine.

Table 4.2. Characteristics of EOS M280 3D printer [99][95]*[74].*

	Min. value	Max. value	Increment
Layer thickness (mm)	20	50	10
Hatch distance (mm)	10	400	10
Scanning speed (mm/s)	50	7000	1
Power input (W)	1	370	1
Substrate temperature (K)	293	373	1
Focus diameter (mm)	100	500	—

Even if the machine is capable of reaching a high speed, several studies have shown that speed must be balanced with laser power to achieve optimal energy density. If is not balanced, speeds that are too low can produce over-melting and excessive thermal deformations, while speeds that are too fast can cause insufficient melting [96]. For that reason, many studies have been conducted to identify optimal printing conditions.

There are different approaches to quantifying energy density depending on the variables in the study. The first model mentioned in this study was used to calculate the input energy density (IED) according to the following Eq. 5.1 [96]:

$$IED = \frac{P}{v\,d} \qquad \textit{Eq. 4.1}$$

Other models consider additional variables to obtain the energy density of the process:

$$E_v = \frac{P}{v\,h\,s} \qquad \textit{Eq. 4.2}$$

The first method of heat exchange occurs via laser–material interaction, which is called Fresnel absorption. The second dominant transfer occurs by plasma or vapor interaction, which after some experiments was shown to have a small effect when compared with the principal method. Therefore, it can be assumed that the absorption of heat is completely accounted for by the principal method [100]. Energy absorption is reduced with increasing particle size. Energy absorption is also related to the irradiance of the powder bed, which also decreases with an increase in particle size [100].

Laser power and scanning speed play different toles in the development of the keyhole. Speed affects the width of the zone and power the depth of the zone, which means that both factors can be optimized to yield a part with better properties.

To obtain a consistent result when comparing the impact of thermal conductivity, the energy density provided by the system was held constant for all scenarios. The initial temperature of the simulations was set according to the reachable parameters of the machine. For this study, the ambient temperature was considered 20 °C, or 293 K. For the simulation, ambient temperature was considered the initial temperature with an increment due to preheating of the machine to 100 °C, resulting in an initial temperature of 373 K.

Time steps greatly influence the computational time of the simulation. Reducing time steps can be a way to decrease the volume of information to process; however, there is a minimum time step that varies depending on the system being studied. For this study, the step time was selected using Abaqus, and thus periods of 10 ms were used to analyze all cases.

Table 4.3. Parameters and values used in the simulations.

Parameter	Value	Reference(s)
Absorption coefficient (W)	0.4	[101]
Average powder diameter (μm)	40	[102]
Coefficient a_r (μm)	220	[97]
Coefficient b (μm)	120	[97]
Coefficient b_r (μm)	60	[97]
Coefficient c (μm)	150	[97]
Gas thermal conductivity (W/m·K)	0.016	[103]
Hatching distance (μm)	140	[99][95][74]
Initial preheated temperature (K)	373	[99][95][74]
Laser diameter (μm)	100	[99][95][74]
Laser power (W)	200	[99][95][74]
Latent heat fusion (J/kg)	273790	[104]
Layer thickness (μm)	60	[99][95][74]
Melting temperature (K)	1643	[105][106]
Sintering temperature (K)	1369	[105][106]
Solid emissivity	0.44	[107]
Speed (m/s)	1, 1.5	[99][95][74]
Time step (ms)	1	[95]

4.3 Results

As can be revealed from Figure 4.5 and Figure 4.6, the laser penetrated the powder bed in a defined distribution. Temperature was filtered to turn elements grey when the temperature reaches or exceeds the melting point, meaning that this part has completely melted. Even if in the last steps of the simulation most of the elements reached the melting point, the way that the material was heated was different. As can be seen in the first laser track, in some cases the laser does not penetrate the entire depth of the powder layer, but subsequent laser paths increase the temperature until the powder reached the melting point.

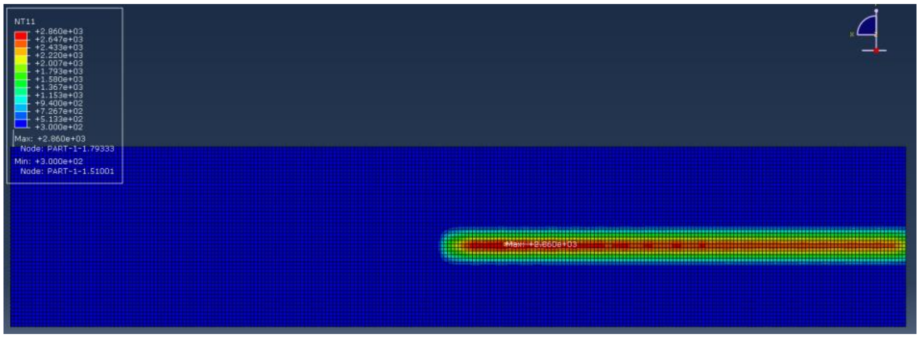

Figure 4.5. Laser scanning the first path in the powder bed.

In order to establish at filtering temperature, temperatures under 1369 K (sintering point was considered 80% of the melting point) were discarded (marked in dark grey), Figure 4.6 and temperatures above 1643 K are depicted in light grey, showing where the material is properly changing phase. There is also a spectrum were the material is only sintered. In the case of the second laser track, the material seemed to heat up faster, and the affected sintered powder expanded.

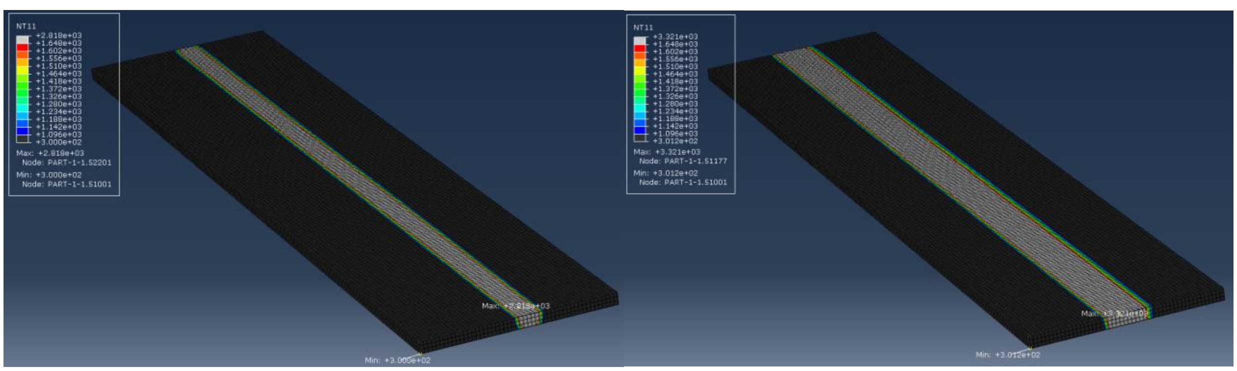

Figure 4.6. Representation of the melting zones in the powder bed. At left, the melting zone is depicted after the laser track was made. At right, the melting zone is depicted immediately after the second laser track was made.

Figure 4.6 also shows the profile of the temperature in the chosen section. A more consistent vertical impact can be seen due to the interaction of the laser with the heated powder. For the first configuration, it can be inferred that the energy absorbed is enough to completely melt the material, and the impact of thermal conductivity is just barely visible.

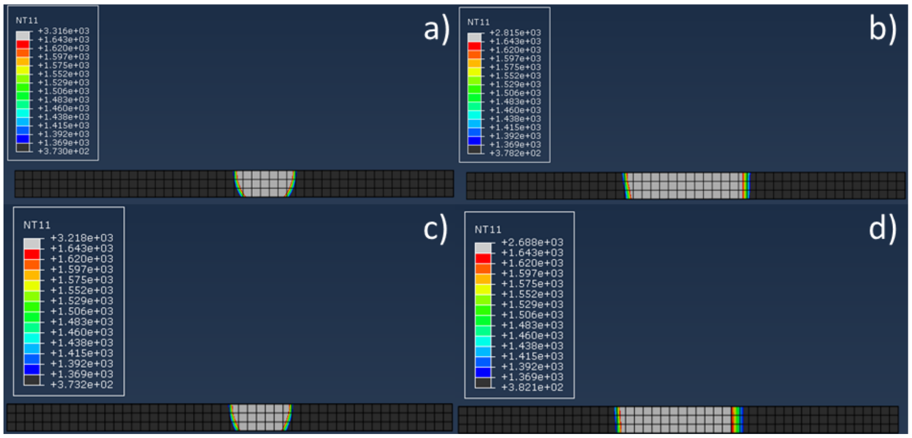

Figure 4.7. Examples of melting pool profiles after the first laser scan (a, c) and second laser scan (b, d). Results are compared using the measured thermal conductivity of compacted (c, d) and non-compacted (a, b) powders. The speed was 1 m/s, and hatching distance is 140 μm.

Figure 4.7 illustrates the differences in thermal conductivity in the most representative cases of compacted and non-compacted powder in the middle section of the part just after the complete first track of the laser. In the case of Figure 4.7, the first path did not mark a clear difference, but the lowest temperature in the powder bed showed an increment of 2 K. In the case of the last step, after 0.005 s of cooling down, the temperature gradient is smaller. In Figure 4.7, melting track comparison shows a decrease in the melting pool of 15 μm and a larger sintering zone. Also, of note is that the second scan penetrated the powder bed in a more vertical orientation, and it propagated more quickly in the surface layer, increasing the melting area in the top surface.

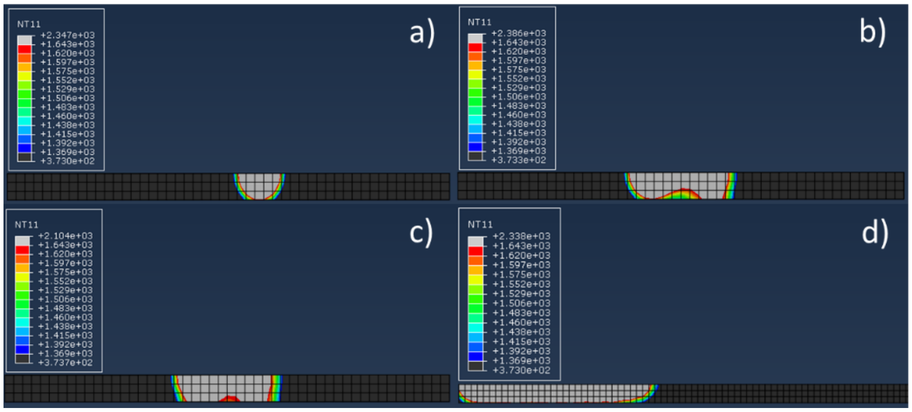

Figure 4.8. Non-compacted thermal conductivity. (a) Section after the first laser path. (b) Section at the second laser path. (c) Section moments after the second laser path. (d) Temperature profile of the laser.

Comparing the visualization of the thermal conductivities in Figure 4.8 (non-compacted) and Figure 4.9 (compacted), the first case shows a very similar thermal distribution. However, in Figure 4.8(b) and Figure 4.9(b), there are important changes when the laser performs its second track. The thermal conductivity of the compacted powder shows a different cooling rate but also a better interaction with close elements. The first track is cooling to the solid state, but is still hot enough to join the second laser track, as shown in Figure 4.8(c) and Figure 4.9(c). Moreover, a lack of fusion can be seen in the bottom of the layer in the non-compacted case.

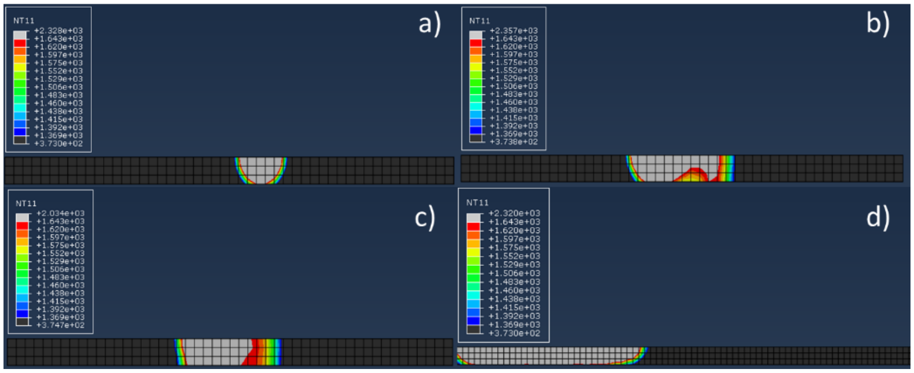

Figure 4.9. Compacted thermal conductivity. (a) Section of the first laser path. (b) Section at the second laser path. (c) Section moments after the second laser path. (d) Temperature profile of the laser.

4.4 Discussion

The effect of thermal conductivity on the printed part shows a better interaction between the laser and the powder bed where there is a more gradual decrement of temperature, that is, in the area closest to the laser track. As a result, the powder close to the laser track is more likely to sinter and not fully melt where not required, such that more accurate dimensions are achieved and postprocessing is easier.

Another important observation is that the temperature gradient decreased during the sintering process. Lower temperatures are highest in the model that uses the thermal conductivity of the compacted powder, and the highest values are lower, meaning that there is better temperature dispersion within the powder bed. This can lead to less evaporation of the material and less residual stress.

Comparing the development of the melting pools and cooling rates shows that lower thermal conductivity leads to more heat being retained in the exact place where the laser passes, while higher thermal conductivity disperses more heat in the rest of the powder bed. Subsequent tracks in the powder bed will therefore already be at a higher temperature, with the advantage that the laser penetrates more deeply, and the material completely melts.

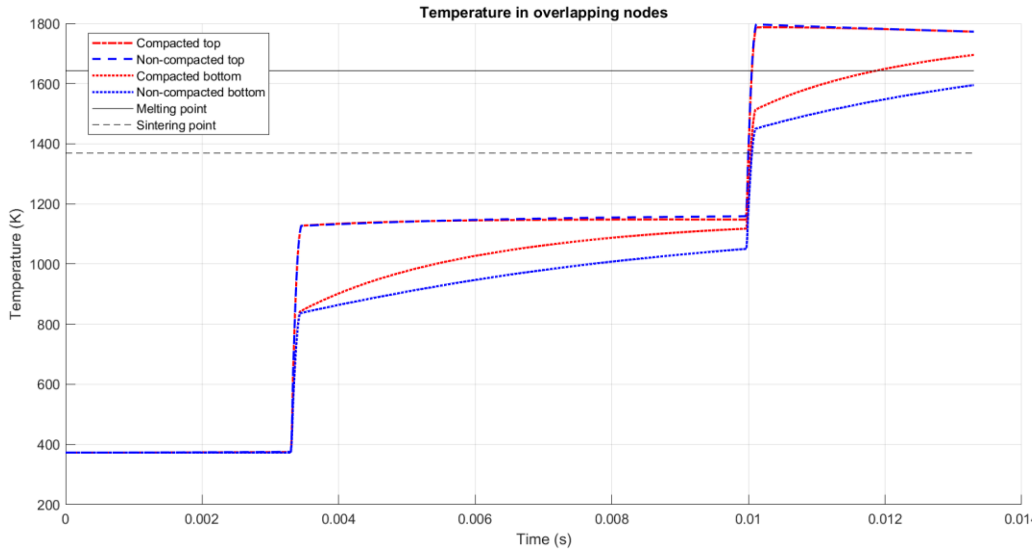

Figure 4.10. Temperature registered from simulation methods in the middle nodes where the laser overlaps.

Figure 4.10 shows the temperature in the top and bottom of the powder bed, which is partially heated in the diameter of the laser. In the two principal steps of the systems, the laser interacts directly with that portion of the powder bed. In the case of the nodes located at the bottom of the powder bed, a delayed effect can be observed. There is a larger gradient in the non-compacted thermal conductivity, while the second track shows much slower propagation, not fully reaching the melting point of the material. Hence, at lower thermal conductivity, the fusion of the new layer with the previous layers is incomplete, because the bonds are not as strong as they are at higher thermal conductivity.

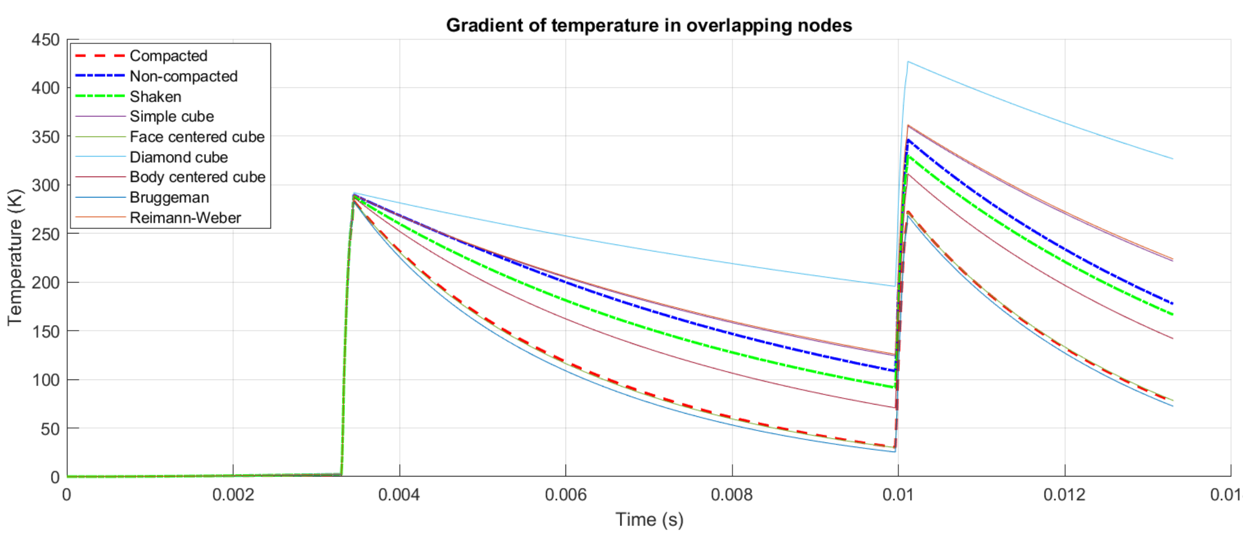

Figure 4.11. Gradient of temperature between the top and bottom nodes, using the different models of thermal conductivity, using the same processing parameters

As mentioned earlier, it is important to reduce the temperature gradient in the powder bed to ensure consistent consolidation of material. Different models of thermal conductivity calculations were then compared with the experimental results (Figure 4.11). Under the same conditions, important variations were observed in the thermal behaviour. As was expected, configurations of powder particles with a higher packing density showed a faster decrement in the temperature gradient after the laser heated the area.

In addition, the temperature in the second track drastically increased the temperature in the top of the powder bed. However, the peak of the gradient temperature at higher thermal conductivities was even slightly lower than for the first track, while the other tracks showed a higher peak and thus a better distribution in a shorter period. Therefore, in comparing the compacted and non-compacted powder beds, an improvement was observed of more than 85 k in the first laser track and more than 100 K in the second laser track.

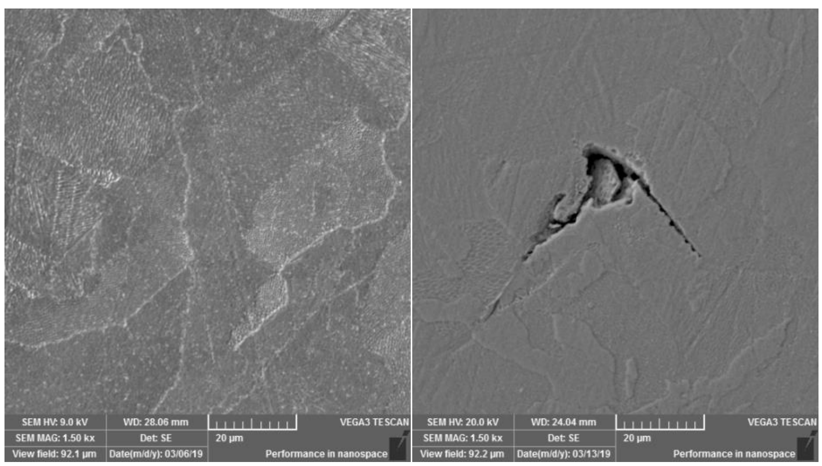

Figure 4.12. Comparison of internal defects in parts manufactured at hatching distance of 140μm, laser power of 250, contrasting the scanning speed of 750mm/s (left), 1750mm/s(right)[108].

Finally, Figure 4.12 is an example to depict results from simulation when a part is build with low energy density, showing the real picture when powder materials are not completely melted. Specimens manufactured in almost the same conditions have very different internal structures. Defects are present in bigger amounts as well as the size of them, when the energy density in the part was lesser. Moreover, it shows poor fusion of particles that propagate to lead to fracture.

4.5 Conclusion

Results revealed that positive effects of better thermal conductivity are more visible when the interaction of the laser and powder bed had a lower energy density. Thus, higher thermal conductivity allows the system to reach a higher printing speed, leading to a final part with superior quality. For that reason, controlling thermal conductivity is one possible approach to increasing the speed and reliability of powder-based processes.

The experimental results related to thermal conductivity showed an important resemblance to the values obtained from numerical models. Even though the compacted powder showed a great deal of similarity to the numerical models, non-compacted thermal conductivities led to the powder behaving in the range of a simple cube and body-centered cube. Moreover, parts simulated using non-controlled powder results are not as low as other particle structures.

Another critical point is the reduction of thermal gradients to improve properties. Higher thermal conductivity reduces the temperature gradients and improves dispersion time. It can potentially reduce residual stresses in the printing process. Moreover, it can also help to decrease the vaporization of the material. Results from the simulation showed that a powder bed with better thermal conductivity reached lower temperatures in the upper layers.

Despite the fact that a higher thermal conductivity can improve thermal distributions, the simulations demonstrated that excessive thermal conductivity could cause unnecessary melting and faster degradation of the powder bed. As a result, the accuracy of the process could decrease, while the operating and postprocessing costs could increase.

Findings shows the benefits of adding mechanisms that maintain a higher packing density in the powder bed in order to increase contact between the particles. Finally, the results of the simulations illustrated the conceptual advantages through the formation of the melting pools. However, a microstructural analysis may be the best way to demonstrate the theorical advantages of optimizing thermal conductivity.

Chapter Five: Conclusions

In this final chapter, a summary of conclusions from each chapter is presented and related to each of the original objectives of this research work. Obtained results here constitute an important contribution to the study of metallic powders used in additive manufacturing (AM) and serve as an innovative foundation for future studies.

5.1 Summary

In AM, a great number of defects are known to compromise the integrity of fabricated parts. Some of these defects, such as porosity and residual stresses, can be attributed to the fusion process. In response to the original research question—How can the fusion process of powder particles be improved? —different approaches were proposed as a solution to theoretically enhance the process in AM.

After designing, building, and testing a method to measure the thermal conductivity of a metallic powder, the effective thermal conductivity of 316L stainless steel (SS-316L) was determined using different methods of powder sampling. The methods were selected based on recreating similar feeding processes that are currently used in the industry. The first sample was taken as a reference with a non-special sampling process, simply the powder deposited in the container, similar to what is found in a gravity feeder. The second sample was compacted to 10% of its initial volume, recreating the roller or blade feeder that generates the compressive force in the powder bed. The third sample was shaken, a method that is more commonly used in molding processes. The findings of the modelling studies are as follows:

- Different powder arrangements significantly altered the thermal conductivity of the SS-316L powder. Compared with the analytical methods, the models showed similarities in some packing densities, but when the powder sample was compacted, the thermal conductivity showed an important increment that was not directly comparable with the analytical results. Improving the packing density of a sample caused the thermal conductivity increment to almost the double, which also resulted in important reduction of gradients of temperature. The lowest thermal conductivity was similar to that of the one calculated at a simple cube representation, but not as low as that of a diamond structure.
- Experiments measured the effective thermal conductivity of different samples reaching temperatures of up to 1000ºC. Overall, thermal conductivity of powdered SS-316L showed an

incremental linear behaviour, at a similar rate of change to that of bulk material but at a significantly lower magnitude.

A finite element simulation model was designed to study and compare the effects of the thermal conductivity of different powder structures. Abaqus v2019 software was selected for the simulation, and subroutines DFLUX and FILM were used to complement the model. The findings were as follows:

- After simulating the propagation of heat, the effective thermal conductivity of different powder structures was compared in overlapping nodes, showing different thermal gradient working at similar rates. Thermal gradients were smaller in powder beds with higher thermal conductivity, giving the theoretical advantage of reducing gradients in solidification, resulting in decrements in residual stresses.
- Simulations of the powder bed fusion process with the results obtained showed that higher thermal conductivity benefited thermal propagation even in short periods. Moreover, it also showed the advantages of low energy density conditions, which transferred enough heat to melt not only the surface but also the bottom of the powder bed.

Benefits of controlling thermal conductivity can lead to get higher mechanical properties. As it was demonstrated in thermal conductivity experiments, gradients of temperature drastically decrease when increasing effective thermal conductivity. Such effects have the potential to be used to control thermal distributions in order to decrease thermal stresses. In addition, a greater propagation of heat would form stronger bonds with surrounding areas of the laser track, reducing risks of failure in manufactured parts.

5.2 Research contributions

Main contributions of the research are as follows:

- Designed a method to safely measure effective thermal conductivity of powders in a steady-state system at high temperatures.
- Showed the beneficial effect of greater thermal conductivity on heat transfer for AM in scenarios with low power density.

Unique elements of the presented work that were not documented before. Such parts are different approaches that may lead to innovation and future research.

5.3 Future research

The current studies of powder fusion and the effective thermal conductivity of SS-316L can serve as the basis for future analyses. Tests and procedures can be improved, as can the addition of different factors. Suggested next research steps are as follows:

- Perform more experiments on thermal conductivity by adding different variables to the experiments: change compression rates, oscillation, controlled atmospheres, particle size distribution, and so on. Then, the number of variables to calculate thermal conductivity would increase the accuracy of the models.
- Create powder models using random and defined distributions to perform Multiphysics simulations. Even if the simulation performed in the research works yields some meaningful results, extended analysis should be performed in order to increase the accuracy of the simulation with more material properties and behaviours. Such simulations will require higher computing power and will consequently drive up computational cost significantly.
- Investigate additional thermal and solidification behaviours of different laser tracks and directions to fully characterize the solidification process in order to obtain more reliable simulations. Then, residual stresses would be determined with greater accuracy, allowing these behaviours to be controlled before processing.
- Finally, apply the learned theoretical improvements to real processes using controlled systems of powder deposition. Then, characterize the mechanical properties and microstructure of the powders to validate and quantify results.

Bibliography

[1] K. V. Wong and A. Hernandez, "A Review of Additive Manufacturing," *ISRN Mech. Eng.*, vol. 2012, pp. 1–10, 2012.

[2] A. Bandyopadhyay and S. Bose, Eds., *Additive Manufacturing*. CRC Press, 2015.

[3] C. L. Ventola, "Medical Applications for 3D Printing: Current and Projected Uses.," *P T*, vol. 39, no. 10, pp. 704–11, 2014.

[4] J. Parthasarathy, "3D modeling, custom implants and its future perspectives in craniofacial surgery," *Ann. Maxillofac. Surg.*, vol. 4, no. 1, p. 9, 2014.

[5] S. Singh, S. Ramakrishna, and R. Singh, "Material issues in additive manufacturing: A review," *J. Manuf. Process.*, vol. 25, pp. 185–200, 2017.

[6] W. E. Frazier, "Metal additive manufacturing: A review," *Journal of Materials Engineering and Performance*, vol. 23, no. 6. pp. 1917–1928, 2014.

[7] H. Lee, C. H. J. Lim, M. J. Low, N. Tham, V. M. Murukeshan, and Y. J. Kim, "Lasers in additive manufacturing: A review," *International Journal of Precision Engineering and Manufacturing - Green Technology*, vol. 4, no. 3. pp. 307–322, 2017.

[8] J. A. Koepf, M. R. Gotterbarm, M. Markl, and C. Körner, "3D multi-layer grain structure simulation of powder bed fusion additive manufacturing," *Acta Mater.*, vol. 152, pp. 119–126, 2018.

[9] E. Klar, P. K. Samal, and ASM International., *Powder metallurgy stainless steels : processing, microstructures, and properties*. ASM International, 2007.

[10] M. Mani, B. M. Lane, M. A. Donmez, S. C. Feng, and S. P. Moylan, "A review on measurement science needs for real-time control of additive manufacturing metal powder bed fusion processes," *Int. J. Prod. Res.*, vol. 55, no. 5, pp. 1400–1418, 2017.

[11] M. Yakout, M. A. Elbestawi, and S. C. Veldhuis, "A Review of Metal Additive Manufacturing Technologies," *Solid State Phenom.*, vol. 278, pp. 1–14, 2018.

[12] "Generative Design at Airbus | Customer Stories | Autodesk."

https://www.autodesk.com/customer-stories/airbus (accessed Apr. 02, 2020).

[13] "Pioneering bionic 3D printing - Company - Airbus." https://www.airbus.com/newsroom/news/en/2016/03/Pioneering-bionic-3D-printing.html (accessed Apr. 02, 2020).

[14] D. Nagy, D. Zhao, and D. Benjamin, "Nature-Based Hybrid Computational Geometry System for Optimizing Component Structure," in *Humanizing Digital Reality*, 2018, pp. 167–176.

[15] "Industrial applications of Renishaw metal additive manufacturing technology." https://www.renishaw.com/en/industrial-applications-of-renishaw-metal-additive-manufacturing-technology--15256 (accessed Apr. 02, 2020).

[16] "Additive manufacturing for healthcare." https://www.renishaw.com/en/--44974 (accessed Apr. 02, 2020).

[17] "Streamlining additive manufacturing for spinal implants." https://www.renishaw.com/en/streamlining-additive-manufacturing-for-spinal-implants--44281 (accessed Apr. 02, 2020).

[18] "Medical and healthcare." https://www.renishaw.com/en/medical-and-healthcare--44309 (accessed Apr. 02, 2020).

[19] "Renishaw AM delivers fast parts at Ferrari F1." https://www.renishaw.es/es/renishaw-am-delivers-fast-parts-at-ferrari-f1--43506 (accessed Apr. 03, 2020).

[20] "SLM Solutions Group AG: Bugatti Develops Functional Components for High-Performance Vehicles with SLM® Technology." https://www.slm-solutions.com/en/industries/automotive/bugatti-develops-functional-components-for-high-performance-vehicles-with-slmr-technology/ (accessed Apr. 03, 2020).

[21] "SLM Solutions Group AG: Bugatti Produces Motor Bracket in Series." https://www.slm-solutions.com/en/industries/automotive/bugatti-produces-motor-bracket-in-series/ (accessed Apr. 03, 2020).

[22] "Additive Manufacturing in the Jewelry Scene - Ganoksin Jewelry Making Community."

https://www.ganoksin.com/article/additive-manufacturing-jewelry-scene/ (accessed Apr. 05, 2020).

[23] "EOS Technology enables Additive Manufacturing of Gold." https://www.eos.info/press/customer_case_studies/glittering_prospects (accessed Apr. 05, 2020).

[24] M. Khan and P. Dickens, "Selective Laser Melting (SLM) of pure gold," *Gold Bull.*, vol. 43, no. 2, pp. 114–121, 2010.

[25] K. R. Bakshi and A. V Mulay, "A Review on Selective Laser Sintering: A Rapid Prototyping Technology." Accessed: Mar. 09, 2020. [Online]. Available: www.iosrjournals.org.

[26] "Direct Metal Laser Sintering [DMLS] Parts On Demand." https://www.stratasysdirect.com/technologies/direct-metal-laser-sintering (accessed Mar. 10, 2020).

[27] "EOS Metal Materials for Additive Manufacturing." https://www.eos.info/material-m (accessed Mar. 10, 2020).

[28] C. Y. Yap *et al.*, "Review of selective laser melting: Materials and applications," *Appl. Phys. Rev.*, vol. 2, no. 4, 2015.

[29] S. Bremen, W. Meiners, and A. Diatlov, "Selective Laser Melting," *Laser Tech. J.*, vol. 9, no. 2, pp. 33–38, 2012.

[30] "Metal Powder Additive Manufacturing Materials from SLM Solutions." https://slm-solutions.us/products/consumables/ (accessed Mar. 26, 2020).

[31] "SLM Solutions Group AG: SLM® Metal Powder." https://www.slm-solutions.com/en/products/accessories-consumables/slmr-metal-powder/ (accessed Mar. 27, 2020).

[32] "About Arcam | GE Additive." https://www.ge.com/additive/who-we-are/about-arcam (accessed Mar. 20, 2020).

[33] M. Galati and L. Iuliano, "A literature review of powder-based electron beam melting

focusing on numerical simulations," *Additive Manufacturing*, vol. 19. pp. 1–20, 2018.

[34] S. M. Gaytan, L. E. Murr, F. Medina, E. Martinez, M. I. Lopez, and R. B. Wicker, "Advanced metal powder based manufacturing of complex components by electron beam melting," *Mater. Technol.*, vol. 24, no. 3, pp. 180–190, 2009.

[35] S. Biamino *et al.*, "Electron beam melting of Ti-48Al-2Cr-2Nb alloy: Microstructure and mechanical properties investigation," *Intermetallics*, 2011.

[36] "LED statt Laser oder Elektronenstrahl: Neue Technologie revolutioniert 3D-Metalldruck." https://www.tugraz.at/en/tu-graz/services/news-stories/planet-research/singleview/article/led-statt-laser-oder-elektronenstrahl-neue-technologie-revolutioniert-3d-metalldruck0/ (accessed May 14, 2020).

[37] A. Dass and A. Moridi, "State of the art in directed energy deposition: From additive manufacturing to materials design," *Coatings*, vol. 9, no. 7. 2019.

[38] A. M. Beese and B. E. Carroll, "Review of Mechanical Properties of Ti-6Al-4V Made by Laser-Based Additive Manufacturing Using Powder Feedstock," *JOM*, vol. 68, no. 3, pp. 724–734, 2016.

[39] H. R. Sandgren, "Characterization of fatigue crack growth behavior in LENS fabricated Ti-6Al-4V using high-energy synchrotron x-ray microtomography," *Addit. Manuf.*, vol. 12, pp. 132–141, 2016.

[40] R. Koike, T. Misawa, T. Aoyama, and M. Kondo, "Controlling metal structure with remelting process in direct energy deposition of Inconel 625," *CIRP Ann.*, vol. 67, no. 1, pp. 237–240, 2018.

[41] "Technical White Paper - HP Metal Jet technology - LS version (Technical white paper/4AA7-3333ENW.pdf)." https://h20195.www2.hp.com/v2/GetDocument.aspx?docname=4AA7-3333ENW (accessed Mar. 25, 2020).

[42] M. Ziaee and N. B. Crane, "Binder jetting: A review of process, materials, and methods," *Additive Manufacturing*, vol. 28. pp. 781–801, 2019.

[43] Y. Zhou, Y. Tang, T. Hoff, M. Garon, and F. Y. Zhao, "The Verification of the Mechanical Properties of Binder Jetting Manufactured Parts by Instrumented Indentation Testing," *Procedia Manuf.*, vol. 1, pp. 327–342, 2015.

[44] A. du Plessis, I. Yadroitsava, and I. Yadroitsev, "Effects of defects on mechanical properties in metal additive manufacturing: A review focusing on X-ray tomography insights," *Mater. Des.*, vol. 187, 2020.

[45] A. Adeyemi, E. T. Akinlabi, and R. M. Mahamood, "Powder bed based laser additive manufacturing process of stainless steel: A review," *Mater. Today Proc.*, vol. 5, no. 9, pp. 18510–18517, 2018.

[46] "Stainless Steels - Stainless 316 Properties, Fabrication and Applications." https://www.azom.com/article.aspx?ArticleID=2868 (accessed Mar. 30, 2020).

[47] H. Zheng *et al.*, "Effect of carbon content on microstructure and mechanical properties of hot-rolled low carbon 12Cr-Ni stainless steel," *Mater. Sci. Eng. A*, vol. 527, no. 27–28, pp. 7407–7412, 2010.

[48] J. Luo *et al.*, "316L stainless steel manufactured by selective laser melting and its biocompatibility with or without hydroxyapatite coating," *Metals (Basel).*, vol. 8, no. 7, 2018.

[49] X. Z. Xin, N. Xiang, J. Chen, and B. Wei, "In vitro biocompatibility of Co-Cr alloy fabricated by selective laser melting or traditional casting techniques," *Mater. Lett.*, vol. 88, pp. 101–103, 2012.

[50] United performance materials, "Stainless 316, 316L, 317, 317L." https://www.upmet.com/sites/default/files/datasheets/316-316l.pdf (accessed Apr. 07, 2020).

[51] T. M. Mower and M. J. Long, "Mechanical behavior of additive manufactured, powder-bed laser-fused materials," *Mater. Sci. Eng. A*, vol. 651, pp. 198–213, 2016.

[52] "Material data sheet-FlexLine." Accessed: Apr. 07, 2020. [Online]. Available: www.eos.info.

[53] Erpro Group, "Material Data Sheet, Stainless Steel 316L / 1.4404 /A276." https://erpro-group.com/wp-content/uploads/2019/04/Fe_316L.pdf (accessed Apr. 07, 2020).

[54] "Understanding 3D Printing Metal Material Nuances | Stratasys Direct." https://www.stratasysdirect.com/materials/metals/understanding-3d-printing-metal-material-nuances (accessed Apr. 07, 2020).

[55] Z. Sun, X. Tan, S. B. Tor, and C. K. Chua, "Simultaneously enhanced strength and ductility for 3D-printed stainless steel 316L by selective laser melting," *NPG Asia Mater.*, vol. 10, no. 4, pp. 127–136, 2018.

[56] S. Natali, A. Brotzu, and D. Pilone, "Comparison between Mechanical Properties and Structures of a Rolled and a 3D-Printed Stainless Steel," *Materials (Basel).*, vol. 12, no. 23, p. 3867, 2019.

[57] R. Penn, "3D Printing of 316L Stainless Steel and Its Effect on Microstructure and Mechanical Properties," Montana Tech, 2017.

[58] D. Gamzina *et al.*, "Additive vacuum electronics: Electron beam melting of copper," *IVEC 2017 - 18th Int. Vac. Electron. Conf.*, vol. 2018-Janua, 2018.

[59] S. K. Everton, M. Hirsch, P. I. Stavroulakis, R. K. Leach, and A. T. Clare, "Review of in-situ process monitoring and in-situ metrology for metal additive manufacturing," *Materials and Design*, vol. 95. pp. 431–445, 2016.

[60] H. Ali, L. Ma, H. Ghadbeigi, and K. Mumtaz, "In-situ residual stress reduction, martensitic decomposition and mechanical properties enhancement through high temperature powder bed pre-heating of Selective Laser Melted Ti6Al4V," *Mater. Sci. Eng. A*, vol. 695, pp. 211–220, 2017.

[61] J. A. Slotwinski, E. J. Garboczi, P. E. Stutzman, C. F. Ferraris, S. S. Watson, and M. A. Peltz, "Characterization of metal powders used for additive manufacturing," *J. Res. Natl. Inst. Stand. Technol.*, vol. 119, pp. 460–493, 2014.

[62] A. F3049 − 14, "Standard Guide for Characterizing Properties of Metal Powders Used for Additive Manufacturing Processes," *F3049 - 14*, pp. 1–3, 2014.

[63] R. A. Miller and M. A. Kuczmarski, “Method for Measuring Thermal Conductivity of Small Samples Having Very Low Thermal Conductivity,” 2009. Accessed: Apr. 28, 2020. [Online]. Available: http://www.sti.nasa.gov.

[64] B. Liu, H. Wang, and Q.-H. Qin, “Modelling and Characterization of Effective Thermal Conductivity of Single Hollow Glass Microsphere and Its Powder,” *Materials (Basel).*, vol. 11, no. 1, p. 133, 2018.

[65] D. Zhao, X. Qian, X. Gu, S. Ayub Jajja, and R. Yang, “Measurement Techniques for Thermal Conductivity and Interfacial Thermal Conductance of Bulk and Thin Film Materials,” *J. Electron. Packag.*, vol. 138, 2016.

[66] L. C. Wei, L. E. Ehrlich, M. J. Powell-Palm, C. Montgomery, J. Beuth, and J. A. Malen, “Thermal conductivity of metal powders for powder bed additive manufacturing,” *Addit. Manuf.*, vol. 21, pp. 201–208, 2018.

[67] A. V. Gusarov and E. P. Kovalev, “Model of thermal conductivity in powder beds,” *Phys. Rev. B - Condens. Matter Mater. Phys.*, vol. 80, no. 2, 2009.

[68] A. V. Gusarov, T. Laoui, L. Froyen, and V. I. Titov, “Contact thermal conductivity of a powder bed in selective laser sintering,” *Int. J. Heat Mass Transf.*, vol. 46, no. 6, pp. 1103–1109, 2003.

[69] T. D. Ngo, A. Kashani, G. Imbalzano, K. T. Q. Nguyen, and D. Hui, “Additive manufacturing (3D printing): A review of materials, methods, applications and challenges,” *Composites Part B: Engineering*, vol. 143. pp. 172–196, 2018.

[70] I. (Ian) Gibson, D. W. (David W. . Rosen, and B. (Brent) Stucker, *Additive manufacturing technologies : 3D printing, rapid prototyping and direct digital manufacturing*. 2010.

[71] G. A. Longhitanoa, M. A. Larosaa, A. L. J. Munhoza, C. A. De Carvalho Zavagliaa, and M. C. F. Ierardia, “Surface finishes for Ti-6Al-4V alloy produced by direct metal laser sintering,” *Mater. Res.*, vol. 18, no. 4, pp. 838–842, 2015.

[72] M. Galba and T. Reischle, “Additive Manufacturing of Metals Using Powder-Based Technology,” in *Additive Manufacturing*, CRC Press, 2015, pp. 97–142.

[73] N. Yüksel, “The Review of Some Commonly Used Methods and Techniques to Measure the Thermal Conductivity of Insulation Materials,” in *Insulation Materials in Context of Sustainability*, InTech, 2016.

[74] EOS, “Material Data Sheet EOS StainlessSteel EOS M290 IndustryLine,” *EOS GmbH - Electro Optical Systems*, 2017. www.eos.info (accessed Jan. 24, 2020).

[75] P. S. . Ghoshdastidar, *3. Steady-State Conduction: Two- and Three-Dimensional Problems - Knovel*, 2nd edition. Oxford University Press, 2012.

[76] D. Q. Kern, *Process heat transfer*. Tate McGraw-Hill Publishing Company, 1997.

[77] P. S. Ghoshdastidar, *5.12.8 Heat Transfer - Knovel*, 2nd Edition. Oxford University Press, 2012.

[78] A. V. Gusarov and E. P. Kovalev, “Model of thermal conductivity in powder beds,” *Phys. Rev. B*, vol. 80, no. 2, 2009.

[79] A. V. Gusarov, T. Laoui, L. Froyen, and V. I. Titov, “Contact thermal conductivity of a powder bed in selective laser sintering,” *Int. J. Heat Mass Transf.*, vol. 46, no. 6, pp. 1103–1109, 2003.

[80] M. Seifi *et al.*, “Progress Towards Metal Additive Manufacturing Standardization to Support Qualification and Certification,” *JOM*, vol. 69, no. 3. Minerals, Metals and Materials Society, pp. 439–455, 2017.

[81] M. Seifi, A. Salem, D. Satko, J. Shaffer, and J. J. Lewandowski, “Defect distribution and microstructure heterogeneity effects on fracture resistance and fatigue behavior of EBM Ti–6Al–4V,” *Int. J. Fatigue*, vol. 94, pp. 263–287, 2017.

[82] A. Yadollahi, N. Shamsaei, S. M. Thompson, and D. W. Seely, “Effects of process time interval and heat treatment on the mechanical and microstructural properties of direct laser deposited 316L stainless steel,” *Mater. Sci. Eng. A*, vol. 644, pp. 171–183, 2015.

[83] R. Martukanitz *et al.*, “Toward an integrated computational system for describing the additive manufacturing process for metallic materials,” *Addit. Manuf.*, vol. 1, pp. 52–63, 2014.

[84] W. E. King *et al.*, “Laser powder bed fusion additive manufacturing of metals; physics, computational, and materials challenges,” *Appl. Phys. Rev.*, vol. 2, no. 4, p. 041304, 2015.

[85] E. J. R. Parteli and T. Pöschel, “Particle-based simulation of powder application in additive manufacturing,” *Powder Technol.*, vol. 288, pp. 96–102, 2016.

[86] E. J. R. Parteli, “DEM simulation of particles of complex shapes using the multisphere method: Application for additive manufacturing,” *AIP Conf. Proc.*, vol. 1542, no. 1, pp. 185–188, 2013.

[87] T. M. Rodgers, J. D. Madison, and V. Tikare, “Simulation of metal additive manufacturing microstructures using kinetic Monte Carlo,” *Comput. Mater. Sci.*, vol. 135, pp. 78–89, 2017.

[88] T. P. Moran, P. Li, D. H. Warner, and N. Phan, “Utility of superposition-based finite element approach for part-scale thermal simulation in additive manufacturing,” *Addit. Manuf.*, vol. 21, pp. 215–219, 2018.

[89] “SIMULIA User Assistance 2019 - Abaqus User Subroutines Guide.” https://help.3ds.com/2019/english/DSSIMULIA_Established/SIMACAESUBRefMap/simasub-c-ov.htm?ContextScope=all&id=1c7cf17e7547405c8541bc882358156d#Pg0 (accessed Jul. 23, 2020).

[90] “FORTRAN,” in *Collins English Dictionary – Complete and Unabridged*, 12th Editi., 2014.

[91] Eugene Loh, “The Ideal HPC Programming Language Maybe it’s Fortran. Or maybe it just doesn’t matter,” *ACMqueue,* vol. 8, no. 6, 2010, [Online]. Available: https://queue.acm.org/detail.cfm?id=1820518.

[92] “SIMULIA User Assistance 2019 - DFLUX.” https://help.3ds.com/2019/english/dssimulia_established/simacaesubrefmap/simasub-c-dflux.htm?contextscope=all (accessed Jul. 23, 2020).

[93] “SIMULIA User Assistance 2019 - FILM.” https://help.3ds.com/2019/english/DSSIMULIA_Established/SIMACAESUBRefMap/simasub-c-film.htm?ContextScope=all&id=cc86a8135a5a481787ad8d7eced80edd#Pg0 (accessed Jul. 23, 2020).

[94] O. B. Kovalev and A. V. Gusarov, "Modeling of granular packed beds, their statistical analyses and evaluation of effective thermal conductivity," *Int. J. Therm. Sci.*, vol. 114, pp. 327–341, 2017.

[95] D. de Moraes and A. Czekanski, "Parametric Thermal FE Analysis on the Laser Power Input and Powder Effective Thermal Conductivity during Selective Laser Melting of SS304L," *J. Manuf. Mater. Process.*, vol. 2, no. 3, p. 47, 2018.

[96] Q. Guo *et al.*, "In-situ characterization and quantification of melt pool variation under constant input energy density in laser powder bed fusion additive manufacturing process," *Addit. Manuf.*, vol. 28, pp. 600–609, 2019.

[97] J. Goldak, A. Chakravarti, and M. Bibby, "A new finite element model for welding heat sources," *Metall. Trans. B*, vol. 15, no. 2, pp. 299–305, 1984.

[98] M. Moradi, M. Ghoreishi, and A. Rahmani, "Numerical and Experimental Study of Geometrical Dimensions on Laser-TIG Hybrid Welding of Stainless Steel 1.4418," *J. Mod. Process. Manuf. Prod.*, vol. 5, no. 2, pp. 21–31, 2016, Accessed: Sep. 04, 2020. [Online]. Available: http://mpmpjournal.iaun.ac.ir/article_579202.html.

[99] "Systems & materials for additive manufacturing with metals." https://www.eos.info/en/additive-manufacturing/3d-printing-metal (accessed Sep. 03, 2020).

[100] Y. Yang, D. Gu, D. Dai, and C. Ma, "Laser energy absorption behavior of powder particles using ray tracing method during selective laser melting additive manufacturing of aluminum alloy," *Mater. Des.*, vol. 143, pp. 12–19, 2018.

[101] Z. Fan, "Numerical modeling of heat transfer and fluid flow in laser metal deposition by powder injection," Missouri University of Science and Technology, 2013.

[102] M. Yakout, M. A. Elbestawi, and S. C. Veldhuis, "Density and mechanical properties in selective laser melting of Invar 36 and stainless steel 316L," *J. Mater. Process. Technol.*, vol. 266, pp. 397–420, 2019.

[103] J. Ning, D. E. Sievers, H. Garmestani, and S. Y. Liang, "Analytical modeling of in-process temperature in powder bed additive manufacturing considering laser power absorption,

latent heat, scanning strategy, and powder packing," *Materials (Basel).*, vol. 12, no. 5, 2019.

[104] H. Liu, "Numerical analysis of thermal stress and deformation in multi-layer laser metal deposition process," Missouri University of Science and Technology, 2014.

[105] C. H. Ji, N. H. Loh, K. A. Khor, and S. B. Tor, "Sintering study of 316L stainless steel metal injection molding parts using Taguchi method: Final density," *Mater. Sci. Eng. A*, vol. 311, no. 1–2, pp. 74–82, 2001.

[106] N. G. Rodkevich, A. V Pervikov, E. A. Glazkova, A. S. Apkaryan, and M. I. Lerner, "Sintering of 316L stainless steel bimodal powder produced by electrical explosion of wires," *Proc. 12th Int. Conf. Mech. Resour. Diagnostics Mater. Struct.*, 2018.

[107] G. Gubareff, *Thermal radiation properties survey : a review of the literature*, 2nd ed. Minneapolis: Honeywell Research Center, 1960.

[108] A. Eliasu, "Microstructural and mechanical integrity of 3d printed 316L stainless steel," York University, 2019.

Appendices

Appendix A, Subroutine code

```
 SUBROUTINE DFLUX(FLUX,SOL,KSTEP,KINC,TIME,NOEL,NPT,COORDS,
1 JLTYP,TEMP,PRESS,SNAME)

 INCLUDE 'ABA_PARAM.INC'

 DIMENSION FLUX(2), TIME(2), COORDS(3)
 CHARACTER*80 SNAME
 DOUBLE PRECISION a,b,Q,pi,v,cf,cr,ff,fr

 T=TIME(2)

 a=0.00012
 b=0.00015
 cf=0.00006
 cr=0.00022
 ff=0.6
 fr=1.4

 Tt=0.0133

 pt=Tt/2

 l=0.01

 Q=200
 R0=0.00005
 R0=R0**2
 PI=3.141593
 V=1.5

 hd=0.00007

 if (T.le.pt) then

 X=COORDS(1)
 Y=COORDS(2)
 Z=COORDS(3)

 X0=0.0
 Y0=-hd
 Z0=0.0

 XC=X0+V*T
 YC=Y0
 ZC=Z0
 E=0.7

 Q=(et*Q*6*(3**0.5))/((a*b)*(Pi**1.5))
 IF (X<=XC) THEN
 IF(((((X-XC)**2)/(cr**2)+((Y-YC)**2)/(a**2)+((Z-ZC)**2)/(b**2))<1)
*   ) THEN
 FLUX(1)=Q*(fr/cr)*EXP(-3*(((X-XC)**2)/(cr**2)+((Y-YC)**2)/(a**2)+
*   ((Z-ZC)**2)/(b**2)))
 END IF
 ELSEIF (X>XC) THEN
 IF(((((X-XC)**2)/(cf**2)+((Y-YC)**2)/(a**2)+((Z-ZC)**2)/(b**2))<1)
*   ) THEN
 FLUX(1)=Q*(ff/cf)*EXP(-3*(((X-XC)**2)/(cf**2)+((Y-YC)**2)/(a**2)+
*   ((Z-ZC)**2)/(b**2)))
 END IF
 END IF

 FLUX(2)=0.0
 end if
```

Appendix B, Input file Abaqus v2019

```
*Heading
 compacted
** Job name: Compacted Model name: powderbed
** Generated by: Abaqus/CAE 2019
*Preprint, echo=NO, model=NO, history=NO, contact=NO
**
** PARTS
*Part, name=Part-1
*Node
      1, 0.00999999978, 0.000500000024, 5.99999985e-05
      2, 0.00999999978, 0.000479999988, 5.99999985e-05
      3, 0.00999999978, 0.00046000001, 5.99999985e-05
      4, 0.00999999978, 0.000440000003, 5.99999985e-05
      5, 0.00999999978, 0.000419999997, 5.99999985e-05
[…]
*Element, type=DC3D8
    1,  257,  206,    2,   53,  256,  205,    1,   52
    2,  258,  207,    3,   54,  257,  206,    2,   53
    3,  259,  208,    4,   55,  258,  207,    3,   54
    4,  260,  209,    5,   56,  259,  208,    4,   55
    5,  261,  210,    6,   57,  260,  209,    5,   56
[...]
*Nset, nset=Set-1, generate
      1,  102204,       1
*Elset, elset=Set-1, generate
     1,  75000,      1
** Section: Section-1-SET-1
*Solid Section, elset=Set-1, material=Compacted
*End Part
**
```

```
** ASSEMBLY
*Assembly, name=Assembly
*Instance, name=Part-1-1, part=Part-1
*End Instance
**
*Nset, nset=Set-25, instance=Part-1-1, generate
      1,  102204,       1
*Elset, elset=Set-25, instance=Part-1-1, generate
     1,  75000,      1
*Elset, elset=_Surf-5_S6, internal, instance=Part-1-1
   101,   102,   103,   104,   105,   106,   107,   108,   109,   110,   111,   112,   113,   114,   115,   116
   117,   118,   119,   120,   121,   122,   123,   124,   125,   126,   127,   128,   129,   130,   131,   132
   133,   134,   135,   136,   137,   138,   139,   140,   141,   142,   143,   144,   145,   146,   147,   148
   149,   150,   251,   252,   253,   254,   255,   256,   257,   258,   259,   260,   261,   262,   263,   264
   265,   266,   267,   268,   269,   270,   271,   272,   273,   274,   275,   276,   277,   278,   279,   280
   281,   282,   283,   284,   285,   286,   287,   288,   289,   290,   291,   292,   293,   294,   295,   296
[...]
*Surface, type=ELEMENT, name=Surf-5
_Surf-5_S6, S6
*End Assembly
**
** MATERIALS
**
*Material, name=Compacted
*Conductivity
 0.348803,  373.15
 0.390663,  473.15
  0.42585,  573.15
 0.501023,  673.15
[…]
*Density
```

```
7954.,   26.85
7910.,  126.85
7864.,  226.85
7818.,  326.85
7771.,  426.85
[…]
*Elastic
 1.95e+11,  0.25,   20.
 1.91e+11,  0.26,  100.
 1.86e+11, 0.275,  200.
  1.8e+11, 0.315,  300.
 1.73e+11,  0.33,  400.
[…]
*Specific Heat
 498.733,   26.85
 512.122,  126.85
  525.51,  226.85
 538.481,  326.85
  551.87,  426.85
[…]
*Material, name="steel "
*Conductivity
 11.5,
*Density
5700.,
*Elastic
200000., 0.3
*Specific Heat
1.,
**
** INTERACTION PROPERTIES
```

```
*Film Property, name=INTPROP-1
10.
**
** PHYSICAL CONSTANTS
*Physical Constants, absolute zero=-273.15, stefan boltzmann=5.67e-08
**
** PREDEFINED FIELDS
**
** Name: Field-1   Type: Temperature
*Initial Conditions, type=TEMPERATURE
Set-25, 373.
** ----------------------------------------------------------------
**
** STEP: Step-1
*Step, name=Step-1, nlgeom=NO, inc=10000000
*Heat Transfer, end=PERIOD
1e-05, 0.02, , ,
**
** LOADS
** Name: BODYFLUX-1   Type: Body heat flux
*Dflux
Part-1-1.Set-1, BFNU, 1.
**
** INTERACTIONS
** Interaction: SURFFILM-1
*Sfilm
Surf-5, FNU, 373., 1.
** Interaction: SURFRADIATE-1
*Sradiate
Surf-5, AVG, 0.0, 0.5652
**
```

```
** CONTROLS
*Controls, reset
*Controls, parameters=time incrementation
8, 10, , , , , , , , ,
*Controls, parameters=field, field=temperature
0.05, 0.5, , , , , ,
**
** OUTPUT REQUESTS
*Restart, write, frequency=0
**
** FIELD OUTPUT: F-Output-1
*Output, field
*Node Output
NT,
*Element Output, directions=YES
HFL, TEMP
**
** HISTORY OUTPUT: H-Output-2
**
*Output, history
*Radiation Output
FTEMP,
**
** HISTORY OUTPUT: H-Output-1
**
*Contact Output
HFLA, HTL, HTLA, SJD, SJDA, SJDT, SJDTA, WEIGHT
*Radiation Output
FTEMP, RADFL, RADFLA, RADTL, RADTLA, VFTOT
*End Step
```